Master Thesis

In-Beam and Decay Spectroscopy of ^{95}Kr

by

Rosa-Belle Gerst

University of Cologne

Institute for Nuclear Physics

23.01.2017

Examiners

Prof. Dr. Jan Jolie

Prof. Dr. Peter Reiter

Abstract

Excited states in ^{95}Kr have been measured at the RIBF at the RIKEN Nishina Center for Accelerator-Based Science via a prompt-delayed correlation analysis of conjoined SEASTAR and EURICA data. Even Sr and Zr nuclei in the A = 100 region show a sudden onset of deformation at N = 60 while the lighter isotopes up to N = 58 are rather spherical. For the even Kr isotopes, it could be shown that this onset of collectivity is fairly smooth. The nuclei with N = 59 neutrons lie just at the border of these phenomena and are therefore of particular interest. In a study of fission fragments at the ILL, an isomeric $(7/2^+)$ state in ^{95}Kr could be identified. The analysis of prompt γ-radiation, observed in DALI2, in coincidence with isomeric transitions identified in the EURICA array provides new information on the nuclear structure above and parallel to the known isomeric state in ^{95}Kr.

Contents

List of Figures

1 Introduction

The goal of this thesis is the identification of excited states in ^{95}Kr. The analysed data was collected during part of the second SEASTAR campaign in May 2015 at the Radioactive Ion Beam Factory at the RIKEN Nishina Center for Accelerator-Based science where currently the world's highest intensity exotic beams are produced.

The second chapter gives a short introduction to different types of nuclear models, namely the single-particle and collective approaches. Additionally, the evolution of nuclear structure in the relevant mass region is addressed. Neutron rich A $\sim$ 100 nuclei have been of particular interest ever since the observation of a sudden shape transition and shape coexistence in strontium and zirconium isotopes. While the lighter isotopes up to N = 58 have a spherical ground state, a strong prolate deformed equilibrium shape is present from N = 60 onwards [1]. For even krypton isotopes it could be shown that the onset of collectivity is rather smooth [2]. Nuclei with 59 neutrons lie just at the border of these phenomena and are therefore of certain interest. Experiments have revealed rather spherical ground states for N = 59 isotopes in this region with deformed bands present at higher energies [3, 4, 5, 6, 7]. In a study of fission fragments at the ILL Grenoble, an isomeric $(7/2^+)$ state at 195.5(3) keV could be identified in ^{95}Kr [8]. In the neighbouring isotones ^{97}Sr and ^{99}Zr, similar low lying isomeric states have been observed with comparable reduced transition probabilities B(E2). Due to this similarity in structure at low energies, a second isomeric state is assumed to exist on top of the $(7/2^+)$ state. This $(9/2^+)$ isomer, which has been observed in strontium [9] and zirconium [7], is expected to be strongly deformed.

In the third chapter, the experimental setup is described in detail. Inflight fission of a ^{238}U beam was used to generate a secondary radioactive ion beam whose particles were separated and identified with the BigRIPS spectrometer [10]. Nucleon-knockout reactions were then induced in the liquid-hydrogen target system MINOS [11] to produce the isotopes of interest. MINOS was surrounded by the Detector Array for Low Intensity Radiation (DALI2) [12] which was used for the prompt γ-ray spectroscopy. The tertiary ion beam particles were identified in a second mass spectrometer, ZeroDegree. For ^{95}Kr, the EURICA HPGe spectrometer [13] was used as an ancillary detector to observe the isomeric transitions. This use of conjoined SEASTAR and EURICA data enables the prompt-delayed gamma analysis for studying excited states on top of the

previously known isomer in addition to the prompt in-beam spectroscopy of transitions parallel to it.

The particularities of the data analysis are treated in the forth chapter of this thesis where an emphasis is put on the particle identification (PID) using the BigRIPS and ZeroDegree spectrometers. A precise particle identification is crucial for a certain assignment of measured transitions to particular isotopes. Since the EURICA and SEASTAR setups use different data acquisition systems, the correct merging of the two data sets is also essential for this analysis. The results of this work are then presented in the fifth chapter. Various new transitions could be identified in ^{95}Kr on top of its $(7/2^+)$ isomer and $\gamma\gamma$-coincidence analyses were conducted to construct a preliminary level scheme. Additionally, full scale Geant4-simulations were performed with the DALI2 data for the determination of transition energies for the different reaction channels populating ^{95}Kr. In the final chapter, a short summary of results is given together with an overview of future plans for the study of ^{95}Kr.

2 Theoretical Background

Since the atomic nucleus was discovered by Ernest Rutherford in 1911, one has sought to explain the many different static and dynamic properties, that arise from the complex nuclear structure, in terms of the interaction between the nucleons. The success has always depended heavily on the advancement of experimental techniques and theoretical interpretations. The understanding of nuclear forces and structure has steadily become more accurate and detailed. For the lightest nuclei, the description of nuclear properties aims at understanding the interactions of all the nucleons that form the nucleus. In heavier nuclei, this undertaking becomes far too complex and nuclear models have to be used to reduce this complexity and describe the nuclear characteristics.

2.1 Nuclear models

There is a variety of nuclear models attempting to explain and predict the many characteristics of nuclear structure. Generally, these nuclear models can be categorised into two groups. On the one hand, there are single-particle models, in particular the shell model, which are successfully used to microscopically describe the evolution of nuclear structure near closed shells with a relatively small valence space. On the other hand, there are collective models which are most successful for nuclei with a large valence space with properties arising from different types of collective motion of the nucleons.

2.1.1 The nuclear shell model

The most commonly used single-particle model is the nuclear shell model. As a basic concept it is very similar to the atomic shell model. Proton and neutron shells are filled following the Pauli principle. Completely filled shells are viewed as an inert core while the valence space, consisting of all orbitals available for the valence nucleons, determines the nuclear properties. A lot of experimental evidence underlines the validity of this approach. The shell closures are marked by sudden changes in nuclear characteristics. The proton and neutron separation energies, for example, experience sharp drops at certain proton and and neutron numbers. These numbers are the so-called magic numbers of nuclear physics: 2, 8, 20, 28, 50, 82, 126. Other experimental evidence

comes from the neutron capture cross-section and the nuclear charge radius which also show sudden and discontinuous behaviour at the same nucleon numbers. The development of the shell model was therefore based on the successful reproduction of the magic numbers [14, 15].
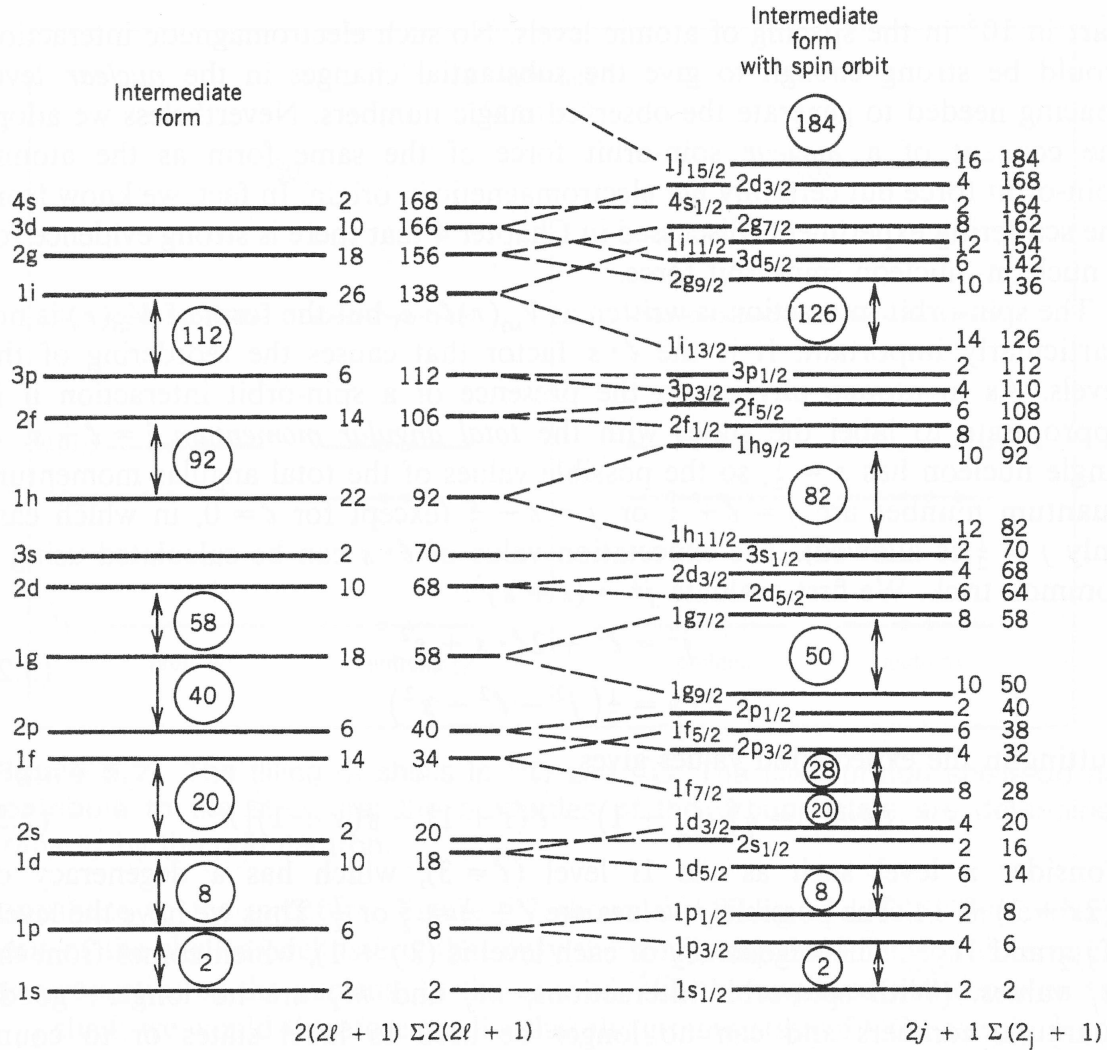
Figure 2.1: The nuclear shell model. On the left, the energy levels were calculated using the Woods-Saxon potential (Equ. 2.1). On the right, the effect of the spin-orbit interaction is shown together with the reproduced magic numbers. Image taken from Ref. [16].

The first approximation of the model is the assumption of the independent movement of nucleons in a central potential representing the average interaction of one nucleon with all the other nucleons. When using a harmonic oscillator as central potential, only the first three magic numbers can be reproduced. Instead, we take the Woods-Saxon potential which combines an infinite well potential with the harmonic oscillator and

presents a more realistic potential shape:

$$V(r) = \frac{-V_0}{1 + \exp\left[(r - R)/a\right]} \, .$$

(2.1)

Here, V_0 represents the potential depth, R the mean radius and a the skin thickness.

Additionally, a spin-orbit term has to be added which again bares resemblance to the corresponding term found in the atomic model. This term takes into account the two possibilities of alignment of orbital and intrinsic spin, namely the parallel and antiparallel arrangement. Due to this spin-orbit coupling, each nl-level splits up into two levels. The state with the lower total angular momentum $j = l \pm s$ (antiparallel) is shifted to higher energies while the one with higher j (parallel) is lowered in energy. Each level has a degeneracy of $(2j + 1)$. Together with the spin-orbit interaction, the Woods-Saxon potential is able to reproduce all magic numbers, as shown in Figure 2.1.

2.1.2 Collective models

While the shell model has proven to be very successful in describing properties in many different nuclei, there exists a wide range of nuclei that need a different approach. Instead of describing the nuclear characteristics in terms of only their valence nucleons, collective models are based on a more macroscopic, unified, behaviour. In 1950, Bohr and Mottelson published a description of collective excitation of nuclei [17] building on the idea of the liquid drop model instead of a shell structure. In this model, the nucleus as a whole is viewed without internal structure. There are two different collective modes of excitation in this picture: harmonic vibrations of the surface of the nucleus around a spherical ground state, and rotation of the elliptical surface of a nucleus with deformed ground state.

l=1   l=2   l=3
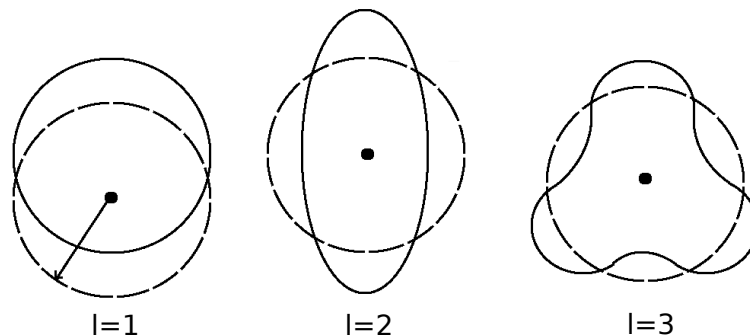
Figure 2.2: The lowest three vibrational modes around a spherical shape (dashed line). A l = 1 dipole vibration is equivalent to a net displacement of the centre of mass and, therefore, does not occur through internal nuclear forces. Image adopted from Ref. [16].

The surface of a nucleus can be written as the expansion of the spherical harmonics:

$$R(\theta, \phi) = R_0 \left[1 + \sum_{l=0}^{\infty} \sum_{m=-l}^{l} \alpha_{lm} Y_{lm}(\theta, \phi) \right].$$

For a permanent deformed nucleus, the coefficients α_{lm} are time independent. For a surface vibration around a spherical ground state, however, they periodically oscillate around zero.

Nuclei can have different vibrational modes. The most commonly found ones are quadrupole vibration with $l = 2$ and octupole vibration with $l = 3$, both shown in Figure 2.2. Vibrational energy is quantised in Phonons, a quadrupole phonon, for example, has $l = 2$.
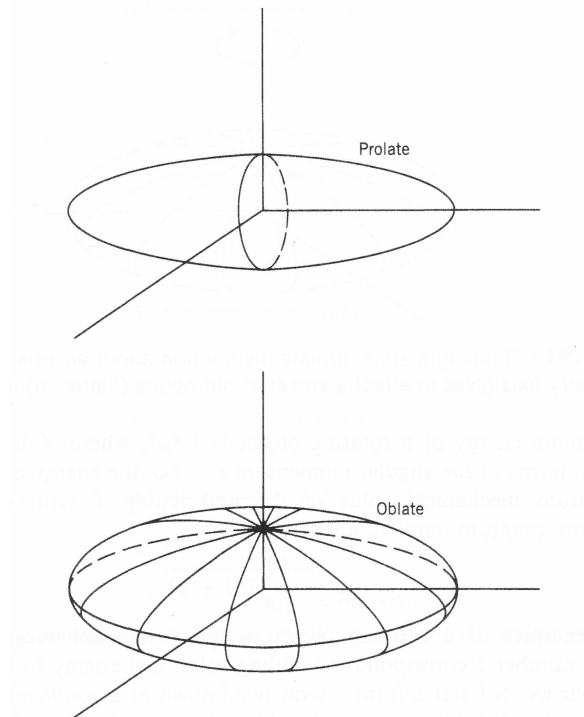
Figure 2.3: Oblate and prolate deformation of nuclei. Image taken from Ref. [16].

For a constant α_{lm}, we have nuclei with deformed equilibrium shapes, commonly represented by a rotating ellipsoid with a surface described by:

$$R(\theta, \phi) = R_0 \left[1 + \beta_2 Y_{20}(\theta, \phi) \right].$$

For the quadrupole deformation parameter β_2, it holds:

$$\beta_2 = \frac{4}{3} \sqrt{\frac{\pi}{5}} \frac{\Delta R}{R_{av}},$$

where ΔR is the difference between the semi-major and semi-minor axes of the ellipse. For negative values of β_2, the nucleus has an oblate, for positive ones, a prolate shape. This is shown in Figure 2.3. The latter is much more prevalent in nature. Besides β_2, quadrupole deformation is also expressed in terms of γ, with $\gamma = 0$ representing prolate deformation, $\gamma = 60$ oblate deformation and $\gamma = 30$ indicating triaxiality.

While quadrupole deformation is the most common type of deformation, nuclei can exhibit a variety of shapes that can be described by combinations of quadrupole and higher order deformation, e.g. octupole, hexadecapole etc..

2.1.3 The Nilsson model

The nuclear shell model is based on the assumption that the nuclear potential is spherical. However, this does not conform with a wide range of nuclei. The Nilsson model was developed to describe single-particle states in axially symmetric deformed nuclei [18]. For these non-spherical nuclei, the shell model potential has to be modified to account for the deformed shape. As a result of the deformation, the orbital angular momentum l and the total angular momentum j are no longer "good" quantum numbers. Thus, states with different l and j values but same parity can mix. In a deformed nucleus, some orbitals are located closer to the bulk of the nucleus than others. The orbitals with less distance are more tightly bound and are therefore lower in energy. For this reason, the level energies depend on the component of j along the symmetry axis of the nucleus. This component is denoted by Ω. A single nucleon occupying an $f_{7/2}$ orbital, for example, has eight possible Ω values, going from $-\frac{7}{2}$ to $\frac{7}{2}$. Due to the axial symmetry of the deformation, the components Ω and $-\Omega$ are degenerate. The $f_{7/2}$ orbital, therefore, splits up into four sub-orbitals each with a degeneracy of two. In a spherical potential, in comparison, we have a degeneracy of $(2j - 1)$, eight in the case of $f_{7/2}$. Figure 2.4 shows the Ω-projections for a prolate deformed and an oblate deformed nucleus.

In an oblate nucleus, the level with the highest $\Omega = j$ has the lowest energy while in a prolate deformed nucleus, this is the case for the level with lowest Ω. The energy spacing between the split states increases with higher deformation of the nucleus. Additionally, the mixing of states with different l and j values gets stronger. In strongly deformed nuclei, the mixing even occurs across major shells. Nilsson model states are illustrated in Nilsson diagrams, with one example shown in Figure 2.5. The states are generally labelled with $\Omega\,[Nn_z\Lambda]$, where N is the principle quantum number, n_z the number of nodes in the wave function in z-direction, and Λ the component of the orbital angular momentum along the symmetry axis.
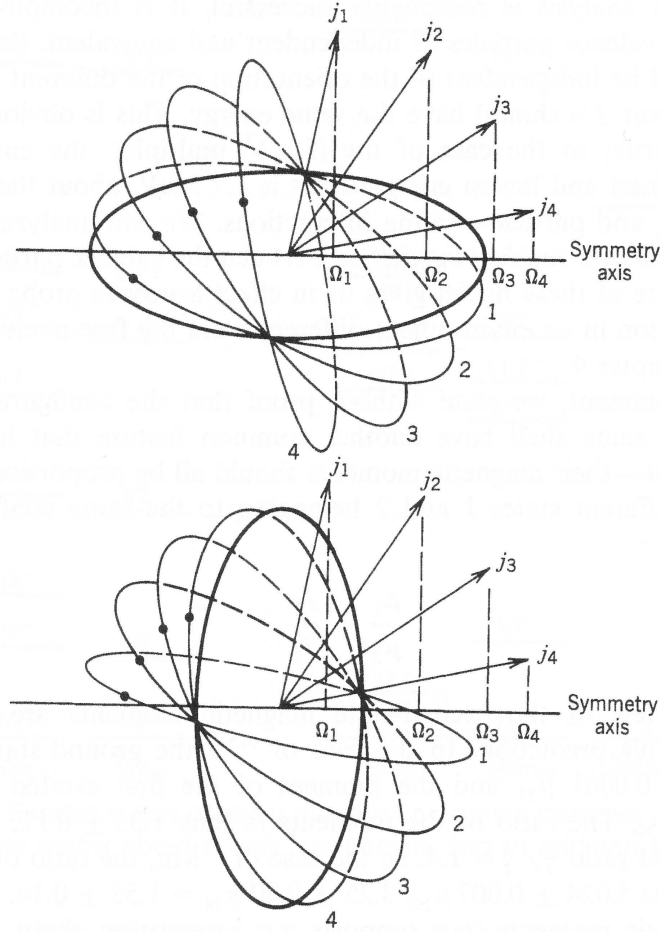
Figure 2.4: Single-particle orbits with j = 7/2 and their possible projections along the symmetry axis for prolate (top) and oblate (bottom) deformed nuclei. Image taken from Ref. [16].

2.2 The $A = 100$ mass region

The A $\sim$ 100 mass region has been of particular interest ever since a very sudden change in ground state shape was observed in even strontium and zirconium isotopes [1]. Ground state properties mostly evolve gradually as a function of proton and neutron numbers with a sudden change of structure normally caused by shell closures marked by the magic numbers. In a few cases though, sharp phase transitions, basically a sudden rearrangement of nucleons, have been observed in mid-shell regions. With increasing neutron numbers, away from the neutron shell closure at N = 50, a transition to deformed ground states is expected due to the growing number of valence nucleons and their correlated excitations. In strontium and zirconium, the ground state shape changes from almost spherical at N = 58 to strong prolate deformation at N = 60, defining a spectacularly sudden onset of deformation. The shape inversion is explained by shape coexistence of a spherical configuration and a strongly deformed one [1]. The former forms the ground state up to N = 58. At N = 60, the deformed configuration
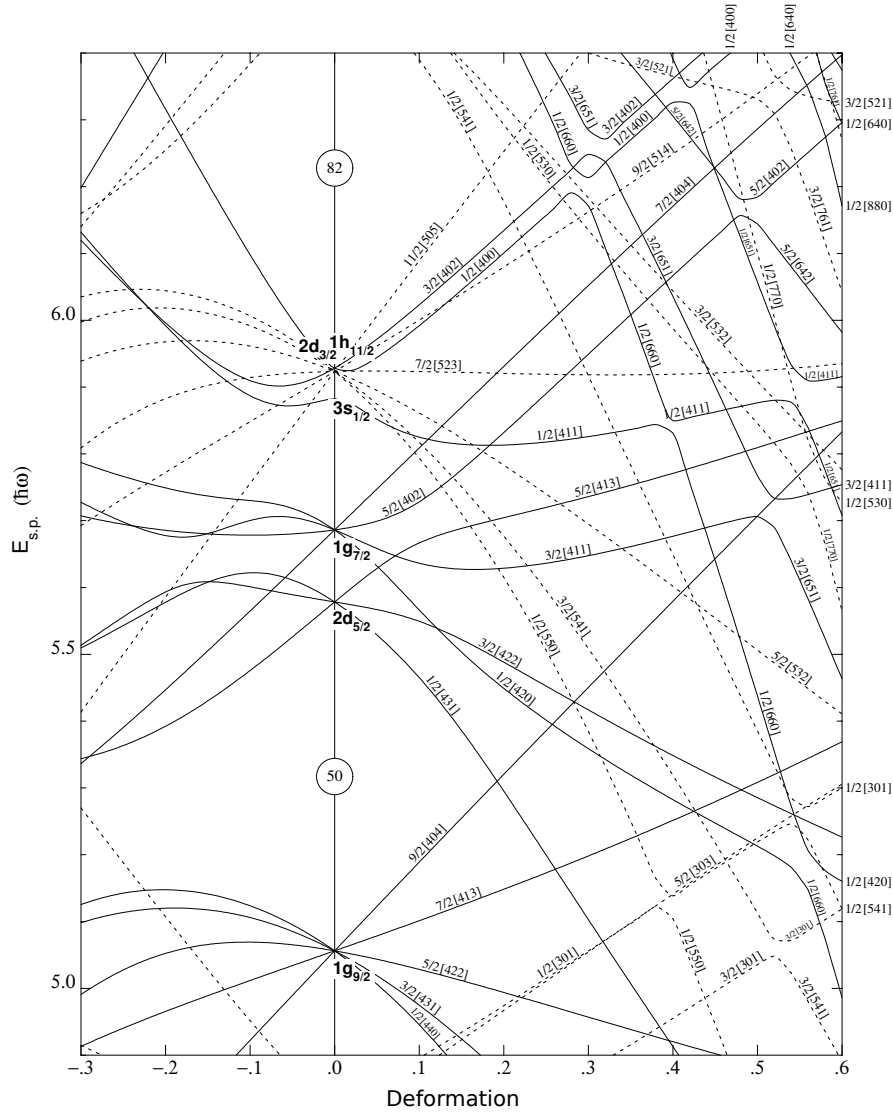
Figure 2.5: Nilsson diagram for neutrons, $50 \leq N \leq 82$. Image taken from Ref. [19].

becomes energetically favourable. Since the sudden onset of deformation of the region is very localised, it is assumed to be caused by certain strongly interacting proton and neutron Nilsson orbitals [9, 21]. The orbitals have a large spatial overlap with a minimum energy at a deformation of $\beta \sim 0.4$. When adding two neutrons to reach $N = 60$, this deformed configuration becomes the ground state with the spherical state coexisting at higher energies. The change in shape is mirrored in the energies of the first excited 2^+-states of the isotopes. The $E\left(2^+\right)$ values are very sensitive to the shell structure. As shown in Figure 2.6, there is a sudden drop in energy when going from the spherical to the strongly deformed ground states in strontium and zirconium. This is expected because a low excitation energy represents a high density of states in the valence space which in turn indicates collective behaviour. For higher Z, the transition to collectivity is more gradual.

Early measurements of even krypton isotopes also indicated a sudden change in ground

15
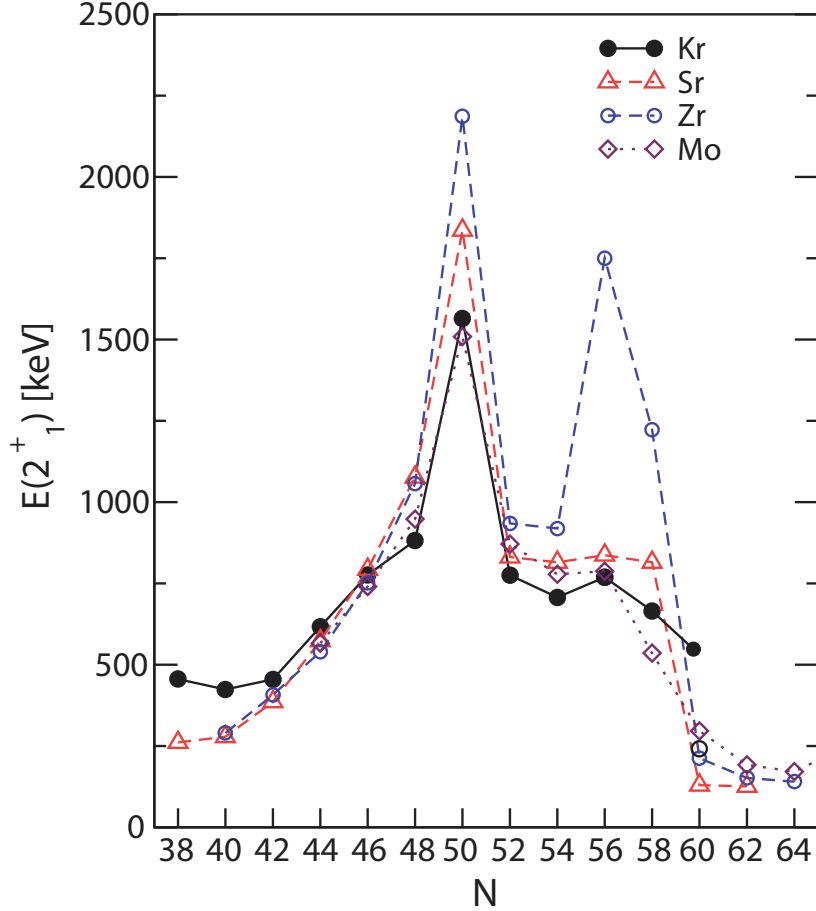
Figure 2.6: $E\left(2^+\right)$ systematics for krypton, strontium, zirconium and molybdenum isotopes. Data taken from Ref. [2, 20].

state shape at $N = 60$ [22]. Later, observations showed a rather smooth phase transition to ground state deformation [2]. This is assumed to be due to the reduced occupation of the highest proton orbital and the, therefore, reduced influence of the deformation driving proton-neutron interaction that causes the sudden onset in strontium and zirconium. Krypton isotopes with $N = 60, 62, 64$ were also measured during the SEASTAR campaign. Preliminary results have shown a continued relatively gradual decrease of $E\left(2_1^+\right)$ values for $N = 62$ and $N = 64$ [23].

2.2.1 $N = 59$ nuclei

As described before, nuclear models are often based on the assumption that either collective or single-particle behaviour dominantly determines the nuclear structure. In even-even isotopes, all nucleons are coupled in pairs and rotational and vibrational collectivity dominates at low energies. In the case of odd-even nuclei, like ^{95}Kr, the unpaired nucleon has to be considered. Thus, their nuclear properties are determined by single-particle and collective effects equally. The $N = 59$ isotones in the $A \sim 100$

mass region are of special interest because they lie right at the border of the prominent change in ground state shape described in the previous section. Experimental data has shown spherical structure for low lying states in ^{95}Kr [8], ^{96}Rb [3], ^{97}Sr [4, 5], ^{98}Y [6] and ^{99}Zr [7]. In all these isotones with the exception of krypton, coexisting prolate deformed states with $\beta \sim 0.3$ were observed above the spherical ground states, while isomeric states were found in ^{95}Kr, ^{97}Sr, ^{98}Y and ^{99}Zr. Furthermore, in strontium and zirconium, a second isomer with spin $9/2^+$ was observed [4, 9]. It corresponds to the neutron-hole excitation from the $\nu 9/2^+[404]$ Nilsson orbital with a maximum deformation of $\beta_2 \simeq 0.44$.
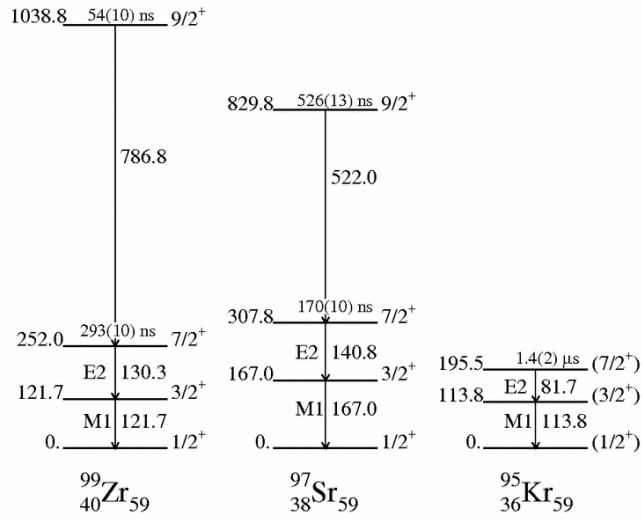
Figure 2.7: Decay schemes of the isomeric transitions in ^{99}Zr, ^{97}Sr and ^{95}Kr. Image taken from [8].

The low lying isomeric state in ^{95}Kr, shown in Figure 2.7, was first observed at an experiment at the ILL reactor in Grenoble studying μs isomers of neutron rich nuclei in the A = 95 chain [8]. A time correlation analysis between the detection of mass-separated fission fragments of ^{241}Pu and γ-rays was performed and two transition energies could be matched to ^{95}Kr: 81.7(2) keV and 113.8(2) keV. Due to the large difference in intensities, different multipolarities were assumed for the transitions. The spin sequence, also shown in Figure 2.7, was assigned due to the similarity in nuclear structure to the neighbouring isotones ^{97}Sr and ^{99}Zr. For the same reason, the multipolarities M1 for the 113.8(2) keV and E2 for the 81.7(2) keV transition were assigned. Due to the similar structure, a second, well deformed $9/2^+[404]$ isomer can also be expected in ^{95}Kr. The second isomer was not observed in Grenoble. The reason for this could be a very low population of the state or a half life too short to be measured due to the flight time between the production target and the experimental setup. With a flight

time of $1.7\,\mu$s, this would require a half-life $< 0.5\,\mu$s . The non-observation could also indicate a single-particle structure differing from ^{97}Sr and ^{99}Zr.

3 Experimental Setup

A new generation radioactive isotope beam factory (RIBF) has been operational at the RIKEN Nishina Center for Accelerator-Based Science since 2007 with the main goal of studying exotic nuclei far from stability. The data, analysed in the course of this master thesis, was taken as part of the second SEASTAR Campaign which concentrated on neutron rich isotopes in the intermediate mass region. Inflight fission of a heavy ion in a light target provides an excellent technique to produce neutron rich nuclei and is better suited than spontaneous fission because the secondary beam can easily be extracted and further processed. At RIKEN, a high intensity uranium beam is used in combination with a beryllium target to provide the highest intensity of exotic beams in the world. The produced particles are separated and identified with the BigRIPS spectrometer and, in our case, delivered to a setup consisting of MINOS (Magic Numbers of Stability) and DALI2 (Detector Array for Low Intensity Radiation 2) which will be described in detail in Sections 3.3 and 3.4. The tertiary beam particles are then identified in the ZeroDegree spectrometer and delivered to the EURICA array where the beam is stopped by a passive stopper.

3.1 Beam production

The primary beam consists of ^{238}U which is produced at the RIKEN superconducting electron cyclotron resonance source (SC-ECR) capable of delivering high-intensity uranium beams [24]. The ^{238}U is accelerated by the RIKEN Linear Accelerator (RILAC) and four different cyclotrons: the RIKEN ring cyclotron (RRC), the fixed-frequency ring cyclotron (fRC), the intermediate ring cyclotron (IRC) and the superconducting ring cyclotron (SRC), which together accelerate the heavy ions up to 345 MeV/nucleon [26]. The accelerator system is displayed in Figure 3.1.

After the acceleration, the beam particles are delivered to a 3 mm thick ^{9}Be production target $\left(555\frac{\text{mg}}{\text{cm}^2}\right)$, located at the entrance of BigRIPS (see Fig.3.2), where the secondary radioactive isotope beams are produced by inflight fission and projectile fragmentation. While not the only method for the production of radioactive ion beams, inflight fission is most successful in delivering neutron rich exotic nuclei [27]. Furthermore, the reaction
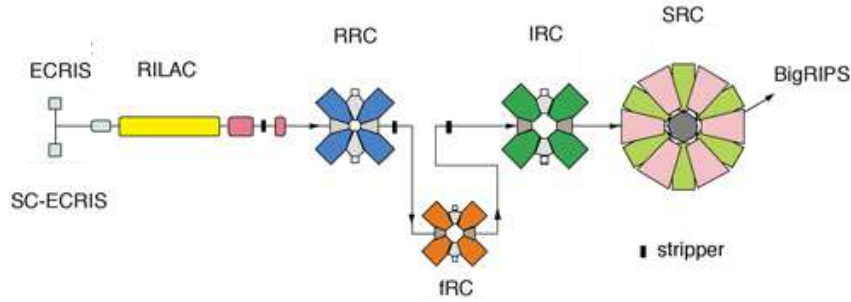
Figure 3.1: The RIBF heavy-ion accelerator system. Image taken from Ref. [25].

products carry a large amount of energy and can easily be extracted, which is especially important for the measurements of short-lived isotopes and isomers.

3.2 BigRIPS and the ZeroDegree spectrometer
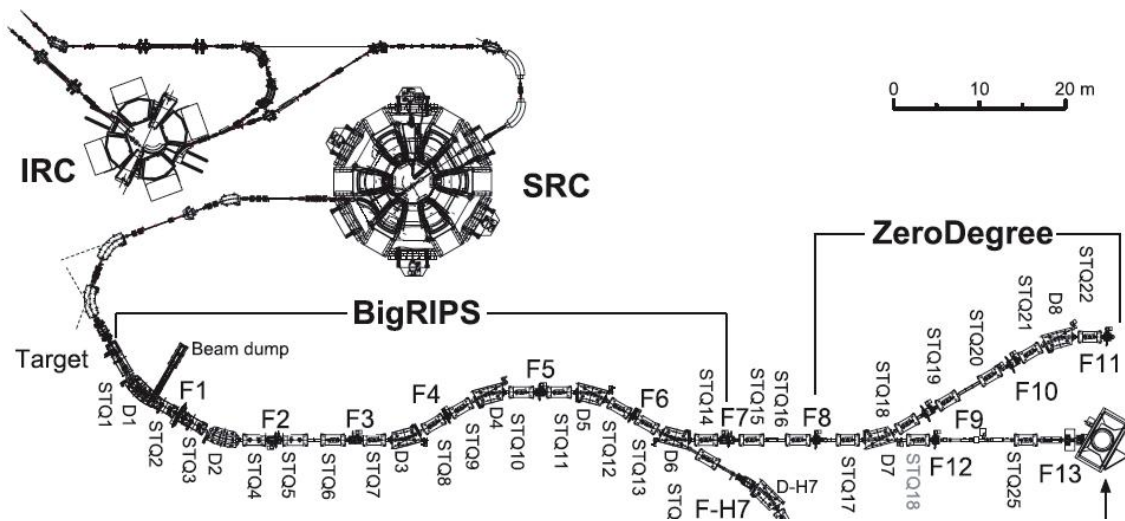
Figure 3.2: The RIBF beam line: BigRIPS and the ZeroDegree spectrometer. Image taken from Ref. [10].

The most essential properties of the two-stage BigRIPS separator are its large ion-optical acceptance and excellent particle identification capability [10]. Especially for inflight fission, in comparison to projectile fragmentation, a large acceptance is of immense value due to the fact that the fission fragments are produced with a large angular and momentum spread. The good resolution of the particle identification is made possible by the two-stage structure. While the first stage is tasked with the production and separation of the radioactive isotope (RI) beams, the second stage is used for their identification.

The BigRIPS separator consists of fourteen superconducting triplet quadrupoles (STQ1-STQ14) and six room-temperature dipoles (D1 − D6) with bending angles of 30°. There are seven focal planes (F1 - F7) arranged over 78.2 m. To achieve a high efficiency of the collection of the fission fragments, the superconducting quadrupoles have a large aperture that provides an angular acceptance of ± 40 mr horizontally and ± 50 mr vertically and a momentum acceptance of $\pm 3\%$ which is of the order of the momentum spread of fission fragments in this energy region. The first stage is composed of D1 − D2 and STQ1 − STQ4 situated between the production target and the F2 focal plane. The second stage, made up by D2 − D6 and STQ7 − STQ14, is located between F3 and F7. The focal planes and beam optics are shown in Figure 3.3.
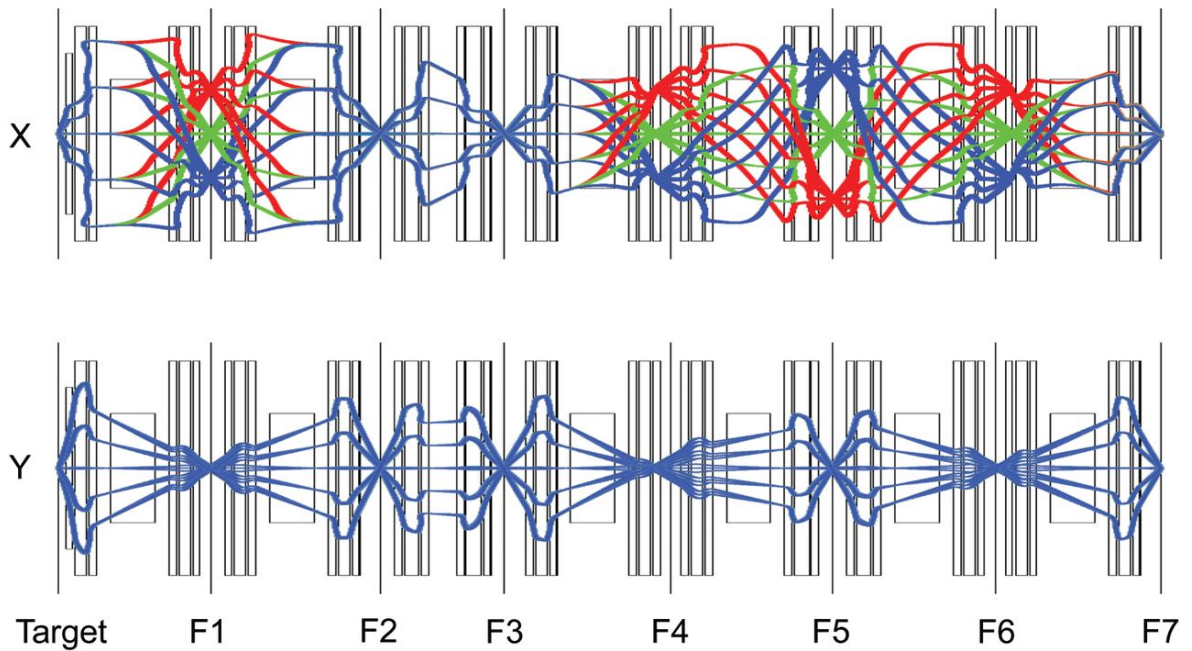
Figure 3.3: BigRIPS Optics. Image taken from Ref. [10].

The first stage separates the secondary beam particles according to their mass-to-charge ratio (A/q) and atomic number. Separation depending to the (A/q)-ratio is generated due to the differing curvatures ρ of the trajectories of the ions in the dipole magnets. Meanwhile, separation depending on the charge Z and in turn on the energy loss is provided by a wedge degrader located at the F1 focal plane. Thus, the beam particles are separated, first, by the bending in the first dipole, then through the energy loss in the degrader and, again, in the second dipole. Therefore, this separation method is called the Bρ-ΔE-Bρ-technique [28]. Bρ = p/q = mv/q is the magnetic rigidity of the particles and reflects their momentum.

The second stage of BigRIPS is responsible for the particle identification which is carried out using the TOF-Bρ-ΔE method. The necessary observables are all measured with various beam line detectors described in the following section. With the TOF,

Bρ and ΔE of the fragments, it is possible to deduce their mass-to-charge ratio and atomic number. An additional energy degrader is located at focal plane F5, to provide the possibility of further beam separation in the second stage.

The ZeroDegree spectrometer consists of two dipoles (D7 $-$ D8) and six superconducting triplet quadrupoles (STQ17 $-$ STQ22) located between focal planes F7 and F11. Similar to BigRIPS, various detectors, placed at the focal planes, are used to calculate A/q and Z of the RI beam particles. An additional advantage of ZeroDegree is that it can be used in different modes depending on the experimental requirements. In the standard mode, it operates with a large acceptance, similar to BigRIPS. When required though, it can also be tuned to achieve better resolution with a smaller acceptance. In our case, with an ancillary experimental setup at F11, the ion optics of ZeroDegree are optimised for the highest possible transmission efficiency.

3.2.1 Particle identification

The separation and identification of particles in BigRIPS and ZeroDegree is performed event-by-event. Different kinds of detectors are installed at the focal planes and are essential for the tuning of the separator and the identification of the beam particles. The TOF-Bρ-ΔE method is used for the identification of the particles. To deduce the (A/q)-ratio, which depends on the curvature of the trajectory of the particles in the dipole magnets, we equate the centripetal force of the circular motion with the magnetic force in the magnetic field of the dipole:

$$\frac{\mathrm{mv}^2}{\rho} = \mathrm{qvB}\,, \tag{3.1}$$

where ρ is the radius of curvature. At the high energies of the accelerator, we are in the relativistic regime. The ion mass m, therefore, transforms to γAu with the Lorentz factor $\gamma = \frac{1}{\sqrt{1-\beta^2}}$ and m $=$ A $\cdot$ u. With the velocity written in terms of the velocity of light, v $= \beta$c, we obtain:

$$\frac{\mathrm{A}}{\mathrm{q}} = \frac{\mathrm{B}\rho}{\beta\gamma\mathrm{uc}}\,. \tag{3.2}$$

Thus, to determine the (A/q)-ratio, the velocity of the beam particles and their radius of curvature have to be measured. The time-of-flight is determined by :

$$\mathrm{TOF} = \frac{\mathrm{L}}{\beta\mathrm{c}}\,, \tag{3.3}$$

where L represents the flight path length and β the particle velocity with $\beta = \mathrm{v/c}$. For the atomic charge, one needs to measure the energy loss of the particles which is

described by the Bethe-Bloch equation:

$$\frac{dE}{dx} = \frac{4\pi e^4 Z^2}{m_e v^2} nz \left[\ln \frac{2 m_e v^2}{I} - \ln \left(1 - \beta^2\right) - \beta^2 \right] \tag{3.4}$$

with the electron mass m_e, the elementary charge e and the atomic number of the beam particle Z. z, n and I correspond to the atomic number, density and mean excitation potential of the material, respectively. Therefore, with the measurement of the energy loss and the velocity of the beam particles, the atomic charge can be deduced.

In BigRIPS, the $B\rho$ is measured once between focal planes F3 and F5, and once between F5 and F7 [28]. The trajectory is reconstructed from the positions and angles measured with Parallel Plate Avalanche Counters (PPAC). The $B\rho$ is measured twice due to the energy loss of the beam particles in the energy degrader located at F5 and the PPACs. From Equations 3.3 and 3.2, we obtain:

$$\text{TOF} = \frac{L_{35}}{\beta_{35} c} + \frac{L_{57}}{\beta_{57} c} \tag{3.5}$$

$$\left(\frac{A}{q}\right)_{35} = \frac{B\rho_{35}}{\beta_{35} \gamma_{35} uc} \tag{3.6}$$

$$\left(\frac{A}{q}\right)_{57} = \frac{B\rho_{57}}{\beta_{57} \gamma_{57} uc} \tag{3.7}$$

where the indices indicate the corresponding focal planes. When no change in A/q occurs at focal plane F5, it holds:

$$\frac{\beta_{35} \gamma_{35}}{\beta_{57} \gamma_{57}} = \frac{B\rho_{35}}{B\rho_{57}} . \tag{3.8}$$

With Equations 3.5 and 3.8, the velocities β_{35} and β_{57} can be calculated, and the A/q values can be determined.

The atomic number Z is deduced from the energy loss ΔE, measured in a Multiple Sampling Ionisation Chamber (MUSIC), and β_{57} using Equation 3.4:

$$Z = C_1 v_{57} \sqrt{\frac{\Delta E}{\ln \left(\frac{2 m_e v_{57}^2}{I}\right) - \ln \left(1 - \beta_{57}^2\right) - \beta_{57}^2}} + C_2$$

with empirical determined calibration parameters C_1 and C_2.

PPACs

Parallel Plate Avalanche Counters [29] are located at focal planes F3, F5, F7, F8, F9 and F11 to measure the particle trajectories. Generally, a PPAC detector consists of two parallel plate electrodes with a constant electric field between them and is filled with gas. The heavy beam ions enter the sensitive area and cause an electron avalanche. Position measurements are performed with a delay-line readout method. A multi-strip cathode electrode connected to the delay-line is used. The position is deduced from the time difference between the two signals from the two ends. The delay-line also prevents pulse pile-up which is necessary for high count rates. At the RIBF, double PPACs are used with two delay-lines, two cathodes and one anode between them. This arrangement increases the detection efficiency significantly. To reconstruct the particle
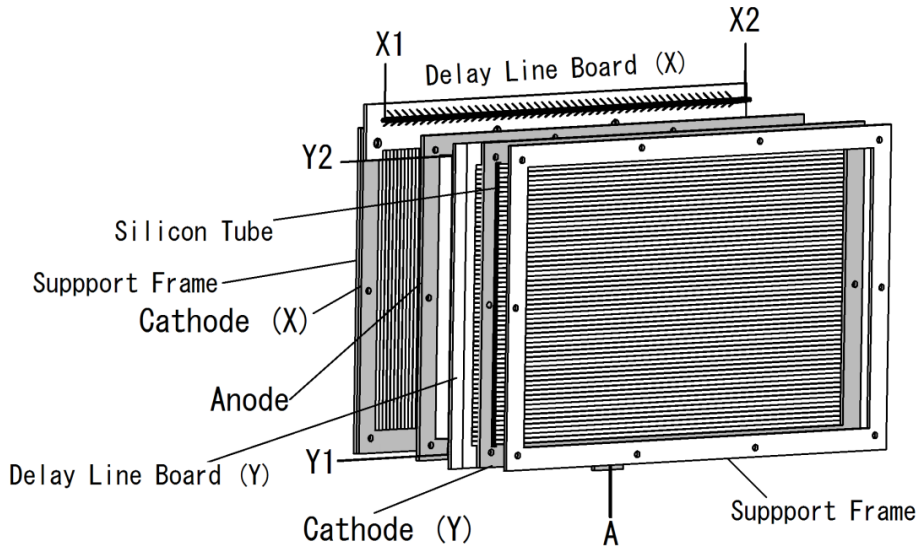
Figure 3.4: Schematic view of the PPAC detector with delay-line. Image taken from Ref. [29]

trajectories, two double PPACs are mounted together at each focal plane.

The positions of the beam particles are calculated with the timing signals of the delay-line:

$$P_x = k_x \frac{T_{x1} - T_{x2}}{2} \tag{3.9}$$

$$P_y = k_y \frac{T_{y1} - T_{y2}}{2} \, ,$$

where T_{ij} are the times the signals need from the interaction point to the different ends of the delay-lines, and k_{ij} time-to-position conversion factors determined in calibration measurements. From this, the magnetic rigidity $B\rho$ is deduced.

Plastic Scintillators

Plastic Scintillators are located at focal planes F3, F5, F7, F9 and F11 and are used for the determination of the time-of-flight. The scintillators have two Photomultiplier Tubes (PMT) on the right and on the left end. The TOF is then calculated with:

$$\text{TOF} = \frac{(\text{StopR} + \text{StopL}) - (\text{StartR} + \text{StartL})}{2} \, , \qquad (3.10)$$

where StartR and StopR are the timing signals from the right PMTs and StartL and StopL from the left one. The velocity of the beam particles is then determined by:

$$\text{v} = \frac{\text{d}}{\text{TOF}} \, , \qquad (3.11)$$

where d is the distance between the two focal planes.

The scintillators are placed at the achromatic focal planes to assure a good time resolution for the TOF measurements.

MUSICs

Multiple Sampling Ionisation Chambers (MUSICs) are used to measure the energy loss of the particles and determine Z at focal planes F7 and F11. The beam particles enter the chamber and lose part of their energy in the filling gas. Their energy deposition is described by Equation 3.4. The MUSICs at the RIBF consist of twelve anodes and thirteen cathodes aligned alternatively. The anodes are connected in pairs and the six anode signals are read out independently to determine ΔE [30]. Events caused by nuclear reactions in the detector or by stopped ions are identified and removed.

In the MUSICs and the PPACs, only the anode signals are read out since the charge collections of the electrons is much faster than that of the slow moving gas ions.

3.3 DALI2

The Detector Array for Low Intensity Radiation 2 (DALI2) was designed for γ-ray spectroscopy with high velocity radioactive ion beams and has been operational since 2002 [12]. It is composed of 186 NaI(Tl) scintillators with a large solid angle coverage with polar angles from ~15° to 160°. During the SEASTAR campaign, the scintillators were arranged in 11 layers around the secondary target, as shown in Figure 3.5. The 1st to 10th layer each consisted of 6 - 14 detectors with two neighbouring layers attached
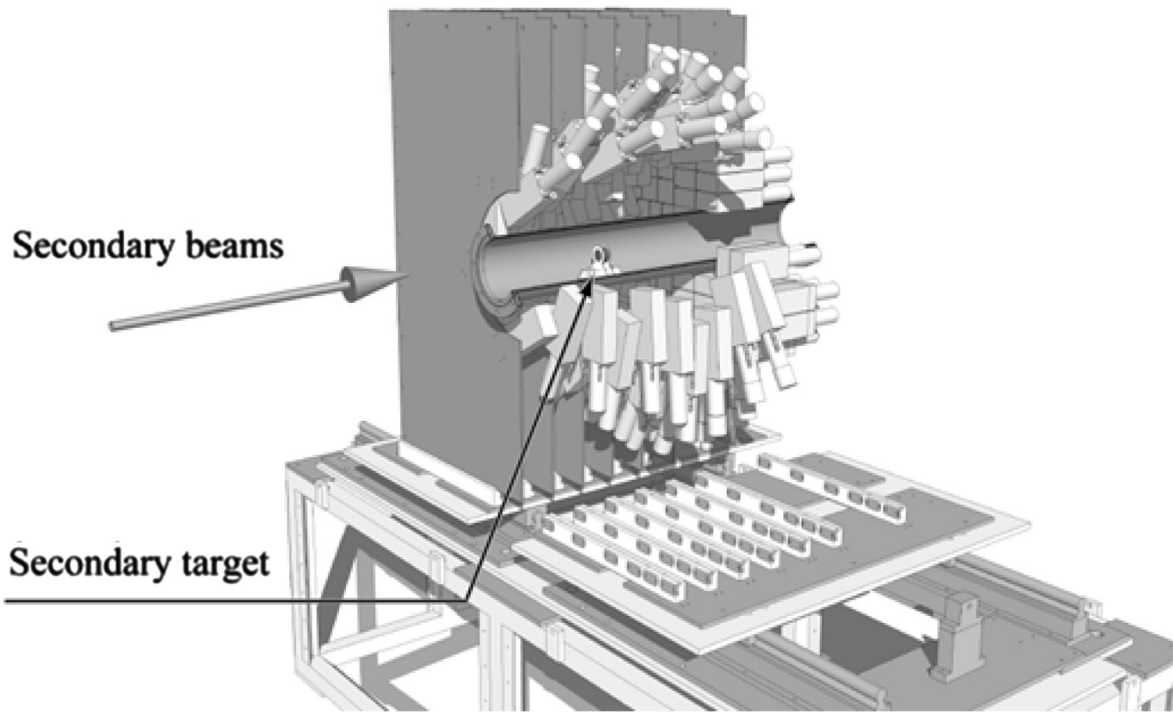
Figure 3.5: Schematic view of the DALI2 detector array. Image taken from Ref. [12].

to the same aluminium plate, as shown in Figure 3.6. Since the emitting particles are moving at high velocity with v $\simeq$ 0.6c , the γ-ray distribution is boosted in forward direction. Therefore, the 11th layer consists of 64 scintillators that cover the forward angles (see Figure 3.6). The measured energies have to be corrected for their Doppler

Figure 3.6: Detector arrangement of DALI2. Top: Layout of 1st to 10th layer, Bottom: Layout for forward angles. Image taken from Ref. [12].

shift because the γ-rays are emitted inflight at high velocity:

$$E_{CM} = E_{lab} \frac{1 - \beta \cos(\theta_{lab})}{\sqrt{1 - \beta^2}} , \qquad (3.12)$$

where θ_{lab} corresponds to the emission angle with respect to the direction of the beam particle, E_{lab} is the measured energy in the lab fr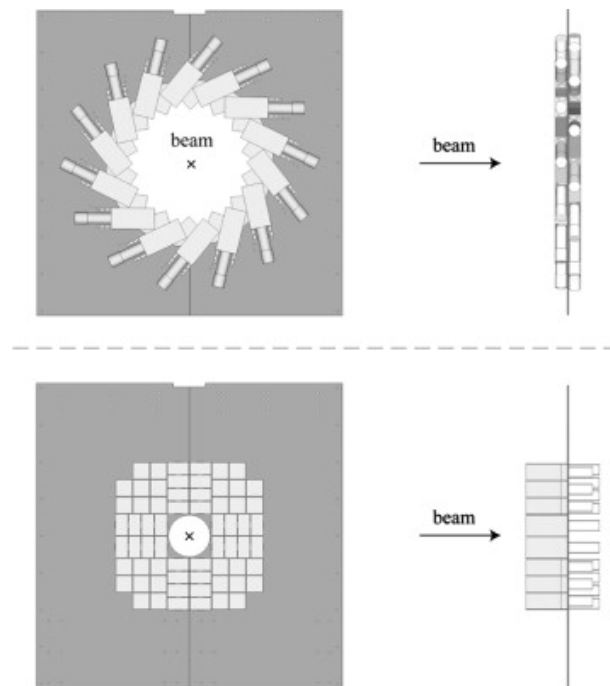ame and $\beta = v/c$ represents the particle velocity. For this reason, the uncertainty of the emission angle and of the beam velocity, as well as the intrinsic detector resolution determine the total energy resolution which is about 10%.

An add-back analysis is done to reduce the effect of Compton scattering and thereby increase the photo peak efficiency. Signals from groups of neighbouring scintillators are added up to deliver the full energy of one γ-ray. The point of first interaction between γ-ray and detector is assumed to have the largest energy deposit and is used for the Doppler correction. This method leads to a significant reduction of the Compton continuum and a considerable increase of photo peak efficiency. For the SEASTAR campaign, simulations with Geant4 [31] provided a photo peak efficiency of 35% (23%) for γ-rays of $500\,keV$ ($1\,MeV$) emitted from the centre of the target with a beam energy of $250\,MeV/u$ [32].

In general, the resolution of the DALI2 spectrometer is adequate for measuring transitions from low-lying states in even-even exotic nuclei. Even-odd nuclei, such as ^{95}Kr, have a large valence space and a correspondingly high level density which make a clear determination and separation of the transition energies difficult with the resolution of the NaI(Tl) scintillators.

3.4 MINOS

At the RIBF, DALI2 is used to measure the prompt γ-decay of the nuclei produced by the reaction of the beam isotopes with the secondary target MINOS, which is located inside the scintillator array. MINOS (Magic Numbers of Stability) consists of a $100\,mm$ thick liquid-hydrogen (LH$_2$) target surrounded by a time projection chamber (TPC) [11]. The secondary beam particles, selected and identified by the BigRIPS spectrometer, undergo nucleon-knockout reactions with the LH$_2$. The prompt γ-decay of the thereby produced excited nuclei are measured in DALI2 while the protons, that are knocked out by the reaction, are detected by the TPC. The tertiary beam particles continue moving in beam direction with a reduced velocity and are delivered to the ZeroDegree spectrometer for identification. A schematic view of the setup is shown in Figure 3.7. When working with very exotic nuclei at relatively low rates, thick targets
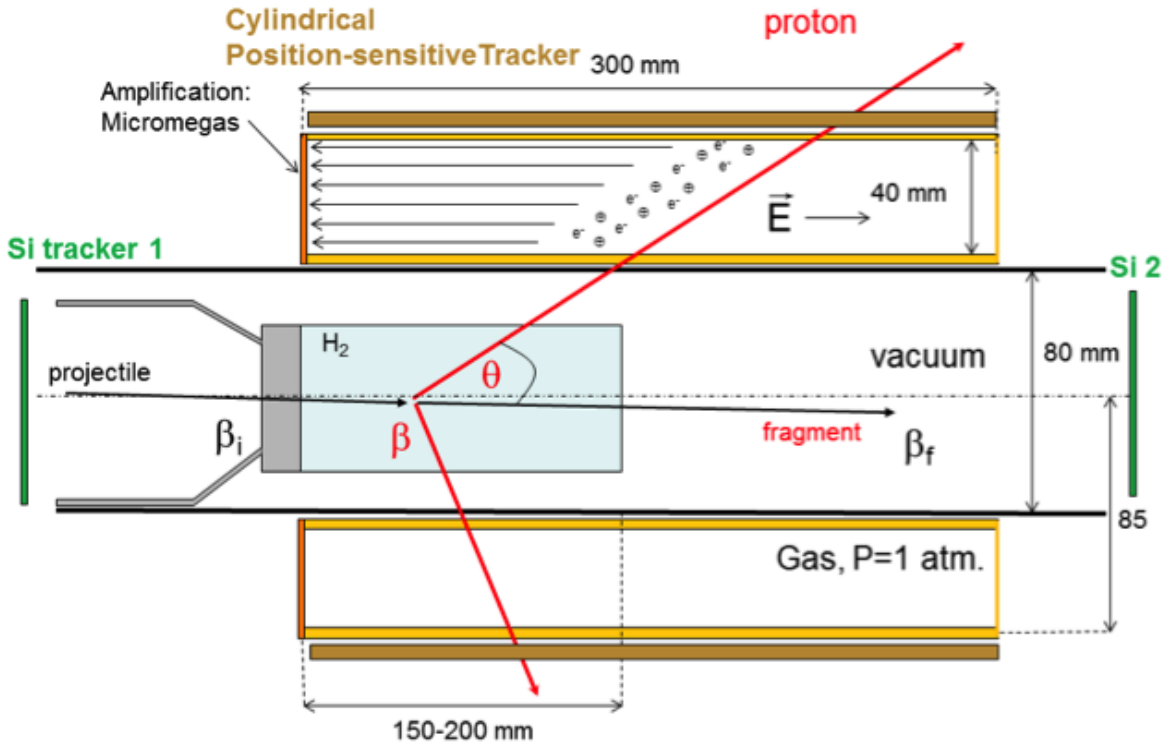
Figure 3.7: Schematic of the MINOS target system, taken from Ref. [11].

are preferably used to increase statistics. As described in the previous section, the precise knowledge of the γ-ray emission angle and the energy loss of beam particles before the emission is essential for an accurate Doppler correction of the measured energies. This becomes problematic in a thick target. For MINOS, this problem is eliminated by the use of the additional time projection chamber which functions as a proton tracker. From the three-dimensional track reconstruction of two or more protons it is possible to determine the reaction vertex position in the target for each observed event separately. A limit to the thickness of the target is set by the probability of a second interaction of the beam particles which have to be identified after the target in the ZeroDegree spectrometer. The length of the target has been optimised for (p, 2p) reactions. For (p,pn) and (p,p') reactions additional position information of the PPACs is used for the reconstruction. With the particle identification provided by ZeroDegree, multiple-reaction events can be removed from the analysis.

The TPC is a concentric cylinder mounted around the hydrogen target with a length of 300 mm to maximise the efficiency of the proton detection. It is filled with gas which is ionised by the protons produced in the nucleon-knockout reactions. An electric field is applied parallel to the beam direction and accelerates the ionised electrons towards the anode and the Micromegas detection plane providing the position information [33].

An additional external Micromegas tracker is placed around the TPC and is used for the determination of the TPC electron drift velocity. With the data from the position sensitive Micromegas detection plane and the measured drift time of the electrons, a three dimensional track reconstruction of the protons is performed. For the data from the SEASTAR campaign, an efficiency of 91 % for vertex reconstruction of (p, 2p) events was achieved with a spatial resolution of $\sigma \simeq 2\,\mathrm{mm}$ [32].

With MINOS situated inside DALI2, together located at focal plane F8 as seen in 3.8, highly sensitive measurements of low-intensity beams of exotic nuclei are possible.
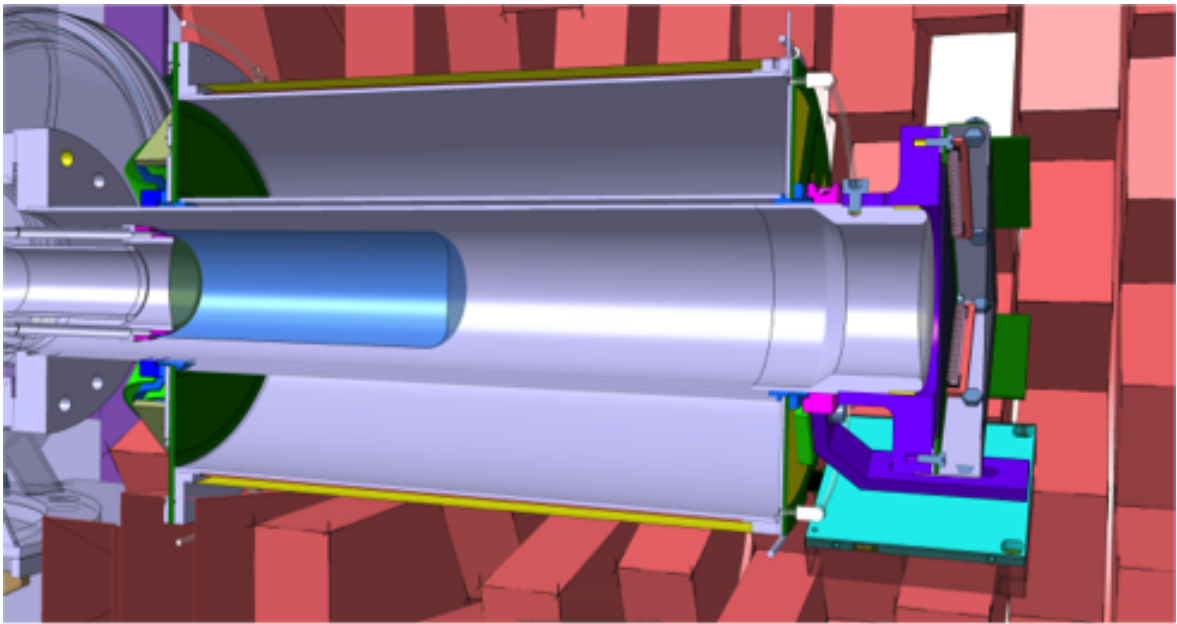

Figure 3.8: 3D drawing of MINOS inside the DALI2 array. Image taken from Ref. [11].

3.5 EURICA

The tertiary beam particles flying after the DALI2-MINOS setup are identified with the ZeroDegree spectrometer and are stopped at focal plane F11 (see Figure 3.2) in an active or passive stopper depending on the experimental requirements. The beam stopper is surrounded by the Euroball RIKEN Cluster Array (EURICA) consisting of twelve High-Purity Germanium cluster detectors [13]. Each cluster contains seven tapered hexagonal HPGe crystals arranged with one central crystal circled by the other six. Previously, these clusters were used in the RISING and PreSPEC campaigns at GSI before they were moved to RIKEN in 2011 together with their stopped-beam electronics and support structure. The clusters are arranged in three rings with two at 51° and 129° containing five clusters each and one at 90° containing 2 clusters (see
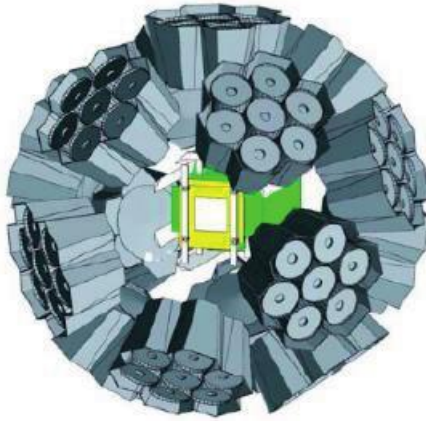
Figure 3.9: Schematic of the EURICA array

Fig. 3.9). The crystals and clusters are packed very closely to increase their solid angle coverage. Similar to DALI2, an add-back analysis is performed. The signals of neighbouring crystals are summed if these signals arrive within a preset time frame and if the sum of the energies is above a preset threshold. The efficiency as a function of γ-ray energy is displayed in Figure 3.10. The peak-to-total ratio of a full energy peak at 1333 keV after add-back is 25.8 % with an energy resolution of 3.17 keV [13].
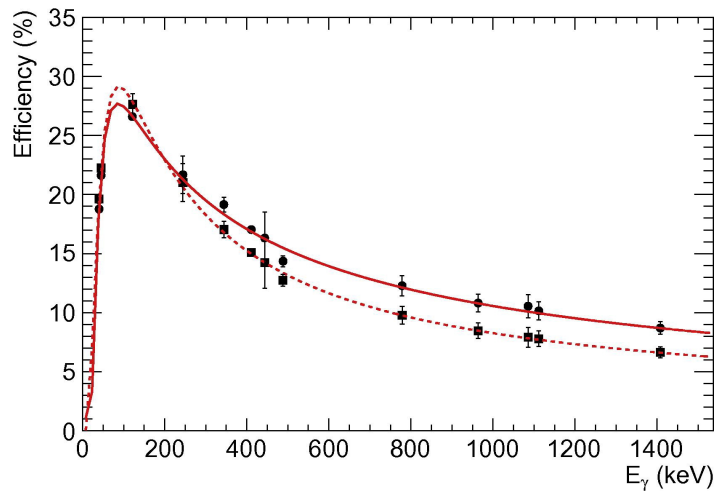

Figure 3.10: Efficiency of the EURICA array with (solid line) and without (dashed line) add-back. Image taken from Ref. [13].

Different ancillary detectors can be placed at the centre of EURICA depending on the experimental requirements, e.g. WAS^{3}ABI for β-decay measurements. For the ^{95}Kr measurements presented in this work, an active stopper was not needed.

4 Data Analysis

There are various important steps that have to be carried out for the data analysis to obtain all quantities of interest. First, the particle identification in BigRIPS and ZeroDegree has to be optimised. A calibrated PID is generated event-by-event from the measurements of the different beam line detectors, as described in Section 3.2.1. Different corrections can be made to improve the resolution of the PID for the nuclei and reactions of interest. Afterwards, all DALI2 and EURICA detectors have to be calibrated. This calibration was not conducted in the scope of this work, but adapted from other participants of the SEASTAR campaign who are analysing data concerning different nuclei.

The energy calibrations of DALI2 were performed by S. Chen (Peking University, RIKEN Nishina Center) using ^{60}Co, ^{137}Cs, ^{133}Ba and ^{88}Y sources. The calibration has an error of 1 keV in the range of $200 - 1500$ keV and an energy resolution of $9\%(6\%)$ (FWHM) at 662 keV (1.33 MeV) [32]. For MINOS, one major uncertainty is the drift velocity of the ionised electrons in the TPC. Their velocity depends on the impurities in the gas and has therefore to be determined for every run. With the drift velocity, the vertex reconstruction algorithm together with the DALI2 data is used to perform the Doppler correction of the γ-ray energies event-by-event. The EURICA detectors were calibrated with a ^{152}Eu source. The calibration was performed by L. Lizarazo (GSI Darmstadt). The calibration files were incorporated in this analysis, their accuracy reviewed and the parameters changed for a few individual detectors for a more precise result.

Another important part of the analysis concerns the merging of the SEASTAR data set, which includes the BigRIPS and ZeroDegree spectrometers, DALI2 and MINOS, with the data set from EURICA which runs on a different data acquisition system. The data, analysed in this work, was taken with two different settings. Data was collected for 33 hours with the transmission through BigRIPS optimised for ^{95}Br and through ZeroDegree for ^{94}Se. Additionally, around two more hours were taken with the ZeroDegree transmission optimised for ^{95}Kr.

4.1 Particle identification

In Figures 4.1 and 4.2, the uncorrected particle identification plots from BigRIPS and ZeroDegree are shown. The following corrections were done for the two different settings of ZeroDegree separately.
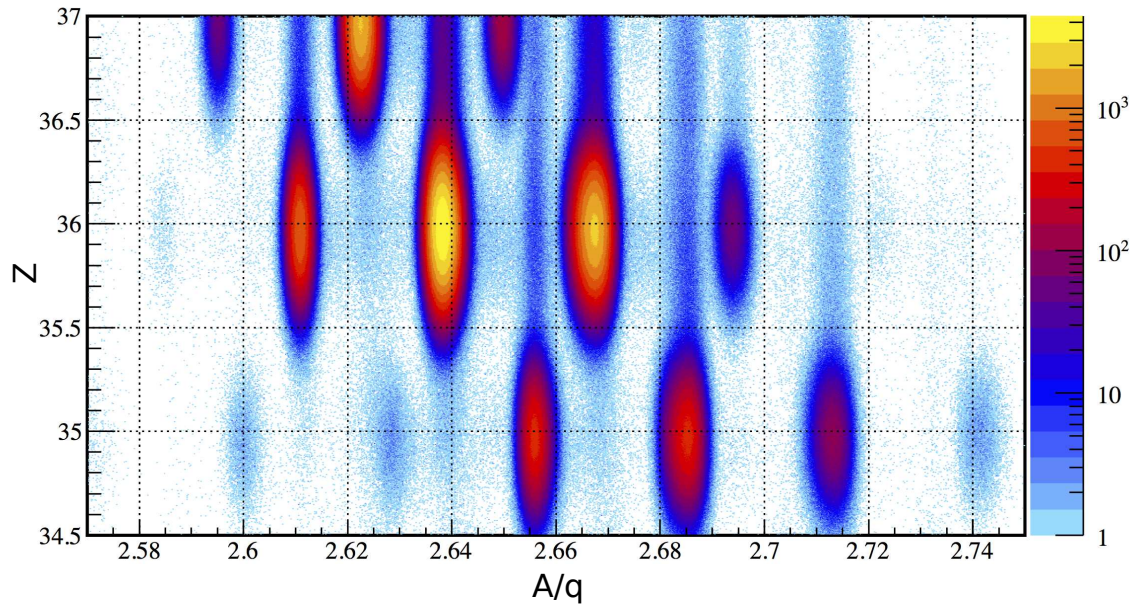
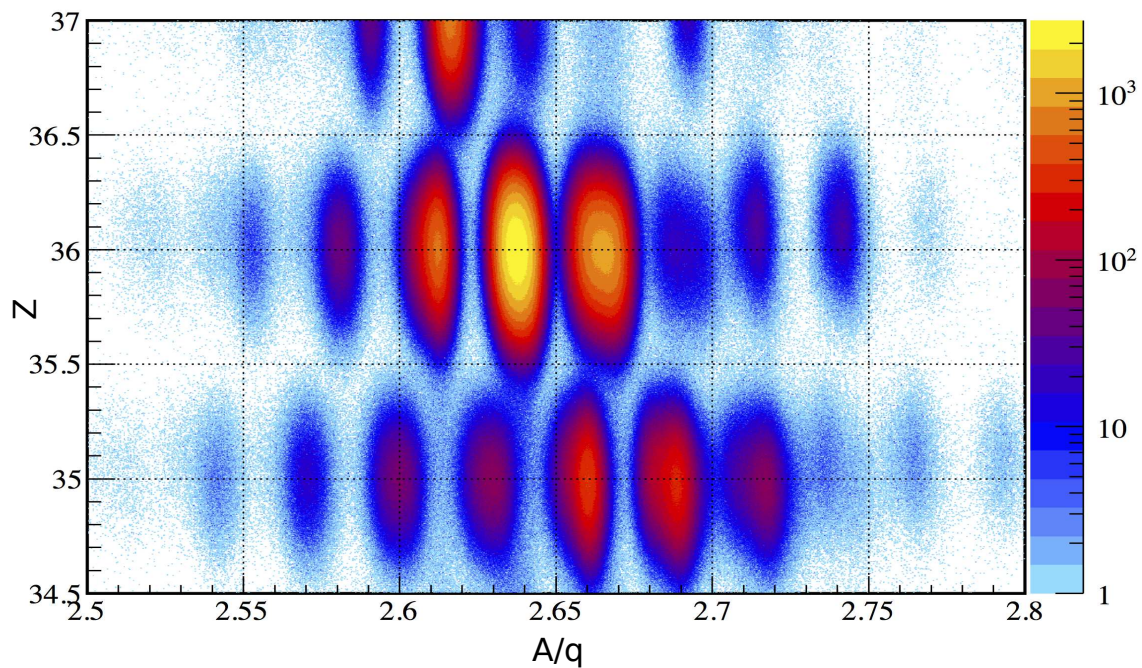

Figure 4.1: Uncorrected BigRIPS PID

Figure 4.2: Uncorrected ZeroDegree PID of the setting optimised for ^{94}Se.

First, the time-of-flight offset has to be optimised to achieve the best A/q value for the nucleus of interest. As described in Section 3.2.1, A/q is determined with the time-of-flight and the magnetic rigidity Bρ. In this case, we want to optimise the PID to an A/q value of 2.6667 for ^{96}Kr in BigRIPS and to 2.6389 for ^{95}Kr in ZeroDegree, as we expect a strong (p, pn) reaction channel. The two offsets for the TOF values between F3-F7 in BigRIPS and F8-F11 in ZeroDegree are modified iteratively until precise A/q values are reproduced.

The ZeroDegree PID can have a slight dependence on the velocity β_{811}. This is corrected optically in a Z-β_{811}-plot to obtain a linear correlation with the correct Z value.

In the next step, we look at the position and angle dependence of A/q. In Figure 4.3, the horizontal position measured at focal plane F9, denoted by F9X, is shown in dependence of A/q. To achieve the required independence, A/q is corrected with
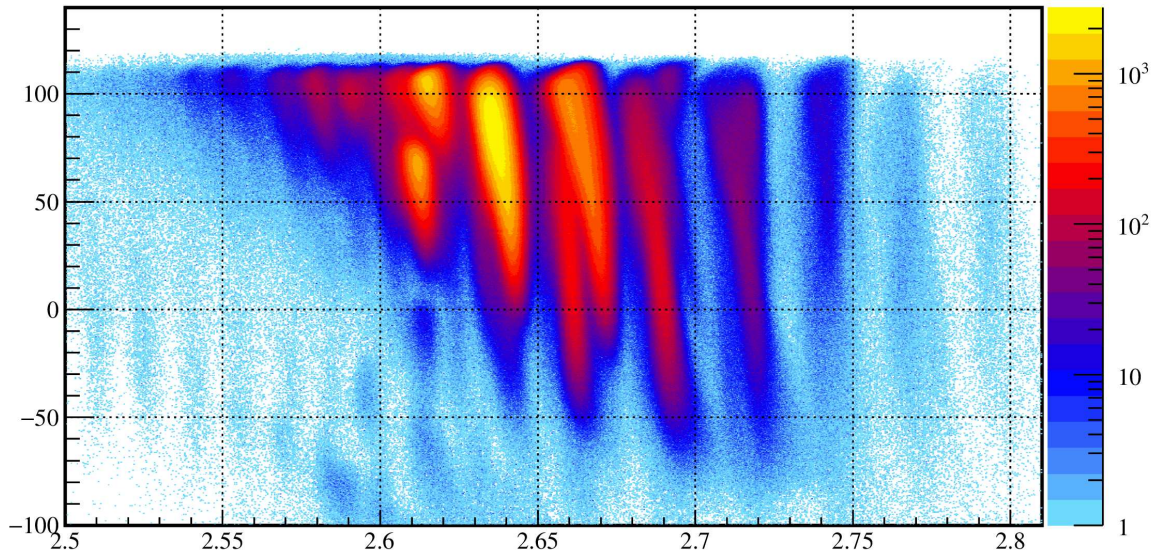
Figure 4.3: F9X position as a function of A/q before corrections.

respect to F9X up to third order. The corrected version is shown in Figure 4.4. These corrections are very localised. While some A/q values show a stronger dependence after the correction, our nucleus of interest, ^{95}Kr for ZeroDegree, displays a linear behaviour. This is done for horizontal positions and angles at focal planes F3, F5 and F7 for BigRIPS once, and for F8, F9 and F11 for the ZeroDegree spectrometer separately for both experimental settings.

For further removal of background events, we look at the different beam line detectors. The plastic scintillators, used for the TOF measurements, have two PMTs connected to the right and left side. The position information of the incident particle is calculated

Figure 4.4: F9X position as a function of A/q after corrections.
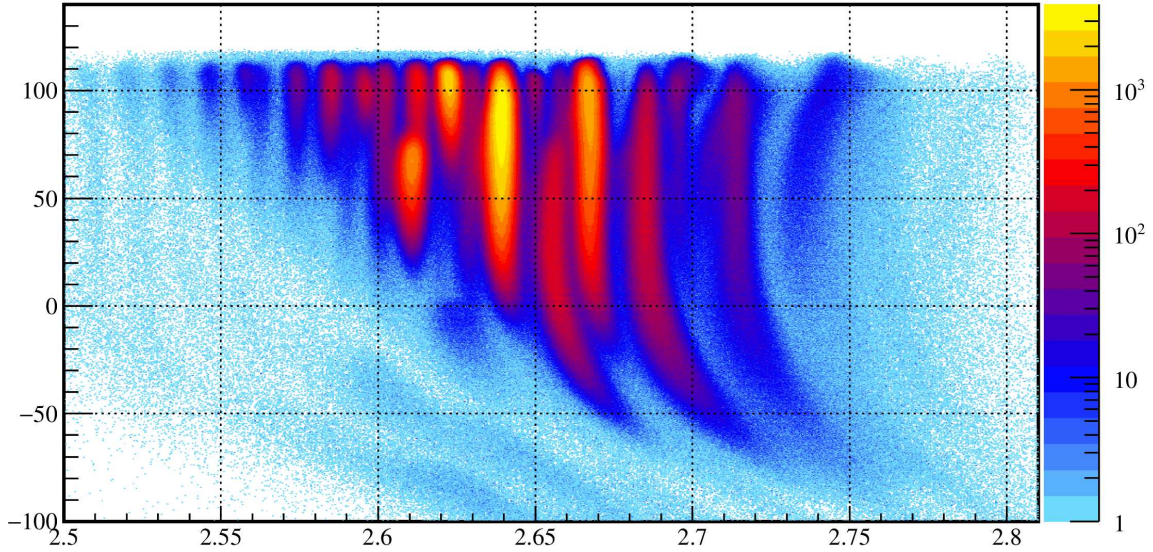
with:

$$x = -\frac{\lambda}{2}\ln\left(\frac{q_1}{q_2}\right) , \qquad (4.1)$$

where q_1 and q_2 correspond to the signals from the two PMTs and λ to the attenuation length of the light in the scintillator. The position information can also be deduced from the timing signals t_i of the PMTs:

$$x = -\frac{V}{2}\left(t_2 - t_1\right) , \qquad (4.2)$$

where V represents the propagation speed of light in the scintillator. From Equations 4.1 and 4.2 we can derive:

$$\lambda\ln\left(\frac{q_1}{q_2}\right) = V\left(t_2 - t_1\right) .$$

In a correlation plot between $\ln\left(\frac{q_1}{q_2}\right)$ and $(t_2 - t_1)$, normal events follow a linear line. Inconsistent events, like charge states differing from 36^+, deviate from the linear correlation and can be removed via two-dimensional cuts in the plot. This is done for the plastic scintillators at F3, F7, F8 and F11.

The PPAC detectors, used for the trajectory reconstruction, are operated with a delay-line, as described in Section 3.2.1, where two timing signals are read out from the two ends. The sum $T_{sum} = T_1 + T_2$ of the two signals has a constant value for normal events. Again, inconsistent events are removed with a corresponding cut.

Additionally, we look at the correlations between detectors at different focal planes. Events, caused by reactions in the scintillators can be removed by comparing the charge-integrated signals and their correlation with ΔE signals from the MUSICs.

The final version of the PID plots from BigRIPS and ZeroDegree is shown in Figures 4.5 and 4.6.
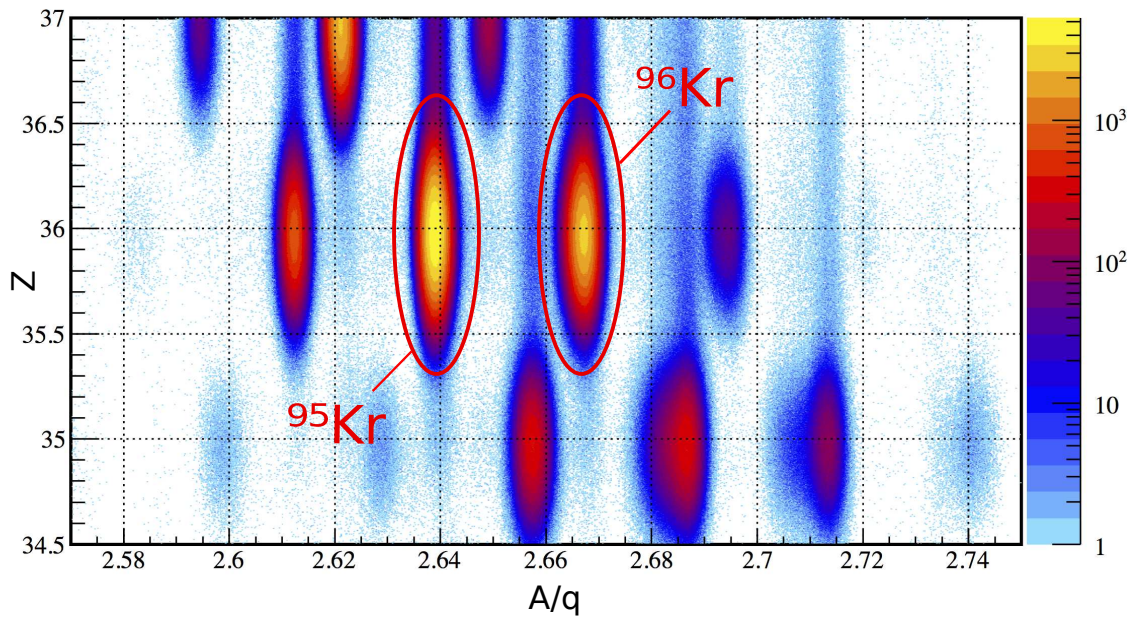
Figure 4.5: Corrected BigRIPS PID

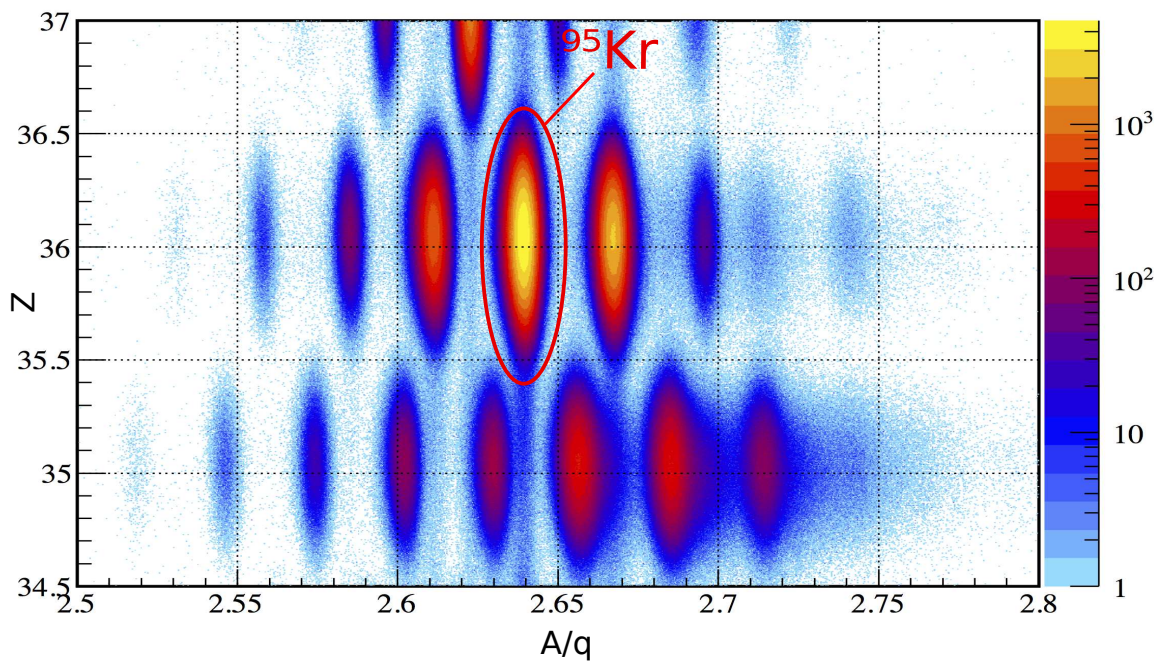**Figure 4.6:** Corrected ZeroDegree PID of the setting optimised for ^{94}Se.

A/q projections of the krypton isotopes in the corrected PID plots are generated with optical cuts and are shown in Figure 4.7 for the BigRIPS (a)) and ZeroDegree (b)) spectrometers. For BigRIPS we see small satellite peaks next to the peaks corresponding to krypton isotopes. These are caused by pile up effects in the MUSIC detector,

also visible in the PID plot in Figure 4.5. For BigRIPS we obtain an A/q resolution of 0.118 % (FWHM), for ZeroDegree of 0.197 % (FWHM).
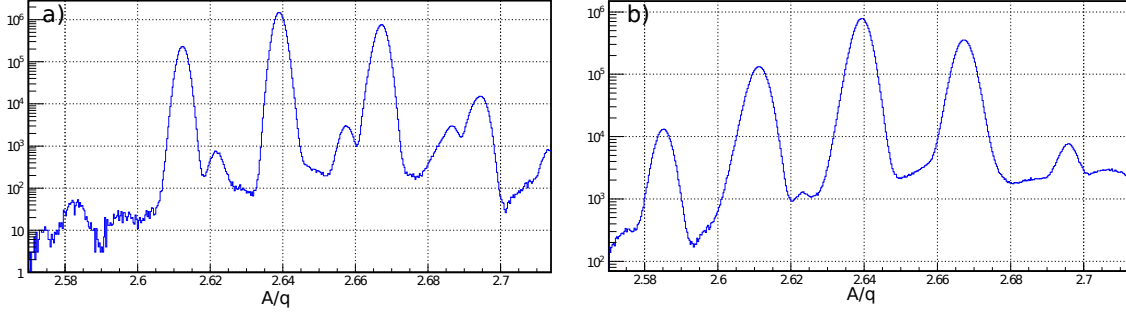
Figure 4.7: PID Projection in A/q for krypton isotopes: a) in BigRIPS and b) in ZeroDegree.

With all corrections implemented, we then put a cut on our nucleus of interest in the ZeroDegree PID plot. With this gate, the remaining BigRIPS PID, shown in Figure 4.8, only includes the nuclei performing reactions with ^{95}Kr as reaction product. In our case, there are three relevant reaction channels: ^{95}Kr $(p, p')^{95}$Kr, ^{96}Kr $(p, pn)^{95}$Kr and ^{97}Rb $(p, 2pn)^{95}$Kr. Therefore, three different data sets are generated for further analysis, each with a different gate in the BigRIPS PID to analyse the three reaction channels separately.

Figure 4.8: BigRIPS PID for a cut on ^{95}Kr in the ZeroDegree PID.

4.2 Trigger

The experimental setup for SEASTAR contained the DALI2, MINOS and beam line detectors. A General Trigger Operator is used to optimise the data acquisition and minimise the dead time. Different triggers were used during the campaign. The downscaled focal plane F7 trigger, DS(F7), corresponds to the incoming beam rate downs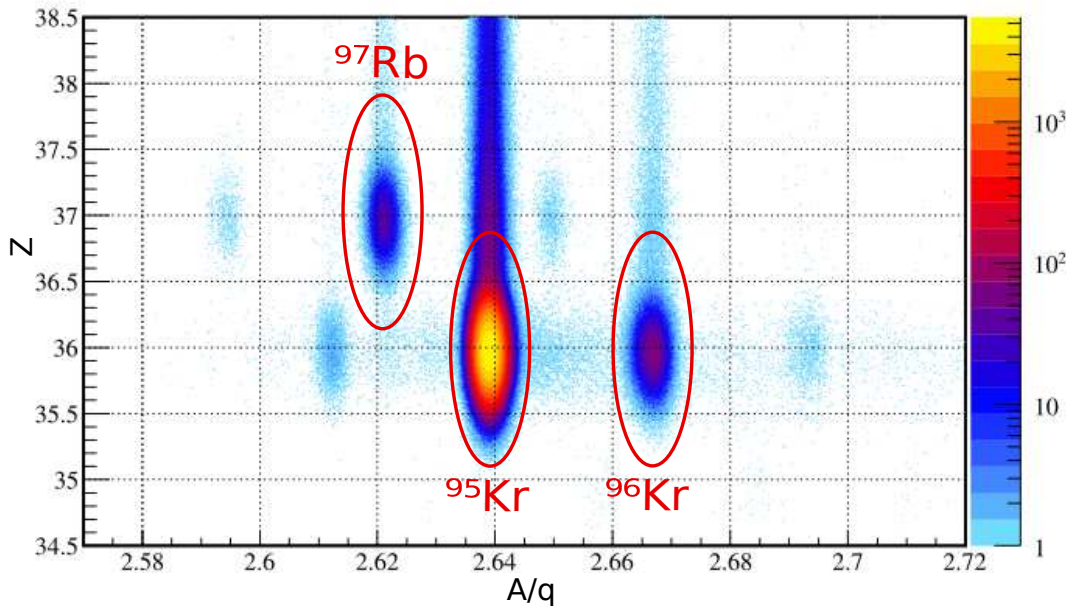caled by a preset factor dependent on the beam intensity. The F7xF11 and the F7xF11xDALI trigger correspond to the incoming beam particles being transmitted to the ZeroDegree spectrometer with or without γ-ray detection in DALI2. Only the DS(F7) and F7xF11xDALI trigger are used to start the data acquisition. For a common dead time of the whole setup, the Trigger Operator always waits for its slowest data acquisition part to continue. In our case, the transmission to ZeroDegree, and accordingly EURICA, has to be guaranteed. Therefore, the F7xF11 and F7xF11xDALI trigger were used with a logic OR gate as conditions during the data analysis. EURICA runs with a trigger system separated from the other parts of the setup. For the combination of the different data sets, the LUPO (Logic Unit for Programmable Operation) timestamp modules are essential [34]. The modules run internal clocks for each detector with a synchronised external clock for the whole system and store the time information of all events.

4.3 Data merging

In the analysis of ^{95}Kr, coincidences between the known isomeric transitions, measured with EURICA, and prompt transitions, measured with DALI2 are of importance. The SEASTAR setup, consisting of BigRIPS, DALI2, MINOS and ZeroDegree runs on a different data acquisition system from EURICA. The former uses the RIBF DAQ [35] and has RIKEN proprietary data output files (ridf). The EURICA data is processed by MBS (Multi Branch System), developed at GSI [36, 37], and has lmd output files. Those files are then processed by Go4 (GSI Object Oriented On-line Off-line system), which outputs root files. Using both data sets together for a prompt-delayed correlation analysis had not been done before. This work, thereby, also presents a first test of this method. For this goal, the two data sets had to be merged with the help of the timestamps generated by the LUPO modules.

During the experiment, it was noticed that the timestamps of the two DAQs were not synchronous, and the LUPO modules were reset to zero. The jump can clearly be seen in Figure 4.9 which shows the EURICA timestamp in dependence of the event number.

Another jump is present at a later point during the experiment, when the beam was gone for approximately one day but the timestamp continued.
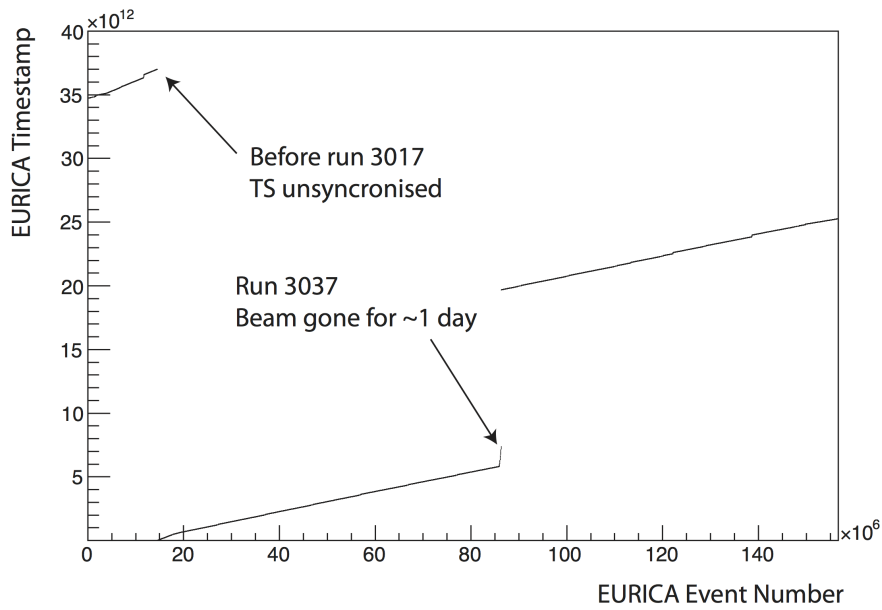

Figure 4.9: EURICA timestamp against event number

The merging algorithm therefore starts by looking for the first recorded event in EURICA after the time reset. Then, a DALI2 event is searched for which lies within a defined time window around the EURICA event. The matched events are combined for further analysis.

5 Results

In this chapter, experimental results of the analysis of ^{95}Kr data are presented. The main focus is set on the prompt-delayed correlation between EURICA and DALI2 to find excited states on top of the $(7/2^+)$ isomer. Additionally, the DALI2 data was analysed separately. The energy spectra of the $(p, 2pn)$ and (p, pn) reaction channels were simulated with Geant4 and a coincidence analysis was performed for both.

5.1 EURICA
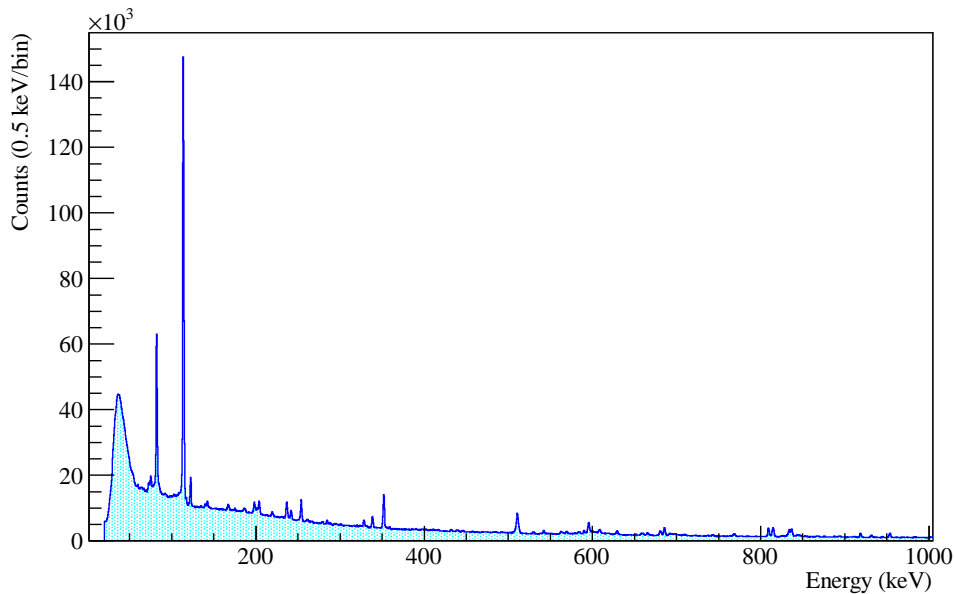
Figure 5.1: Calibrated EURICA energy spectrum for all reaction channels after data merging

In Figure 5.1, we can see the calibrated EURICA energy spectrum after the data merging. The two known transitions from ^{95}Kr at $113.8\,$keV and $81.7\,$keV are the strongest two peaks and can easily be identified. There are also several other, weaker lines. To investigate if any additional peaks belong to the ^{95}Kr isotope, a background subtraction was performed. For this purpose, the energy-time matrix was gated to show the measured energies present before implantation of the ions in the EURICA stopper. This is possible because the trigger of the EURICA data acquisition is generated from

the scintillator signal at the focal plane F11 instead of at the stopper. This background spectrum was scaled accordingly and subtracted from the full energy spectrum. To further minimise background events, we also reduced the prompt flash at low energies by setting a time window starting 100 ns after the ion implantation. Finally, we receive the spectrum shown in Figure 5.2. Only the two known isomeric transitions of ^{95}Kr are left. As discussed in Section 2.2.1, a second isomer is expected to exist on top of the $(7/2^+)$ isomer. Since a transition from this state is not observed in the EURICA spectrum, we can assume that the state is either not populated with a rate high enough to be detected, or has a lifetime too short for the experimental setup. With a flight time of 240 ns through the ZeroDegree spectrometer, this would indicate a lifetime of $T_{1/2} \lesssim 100$ ns.
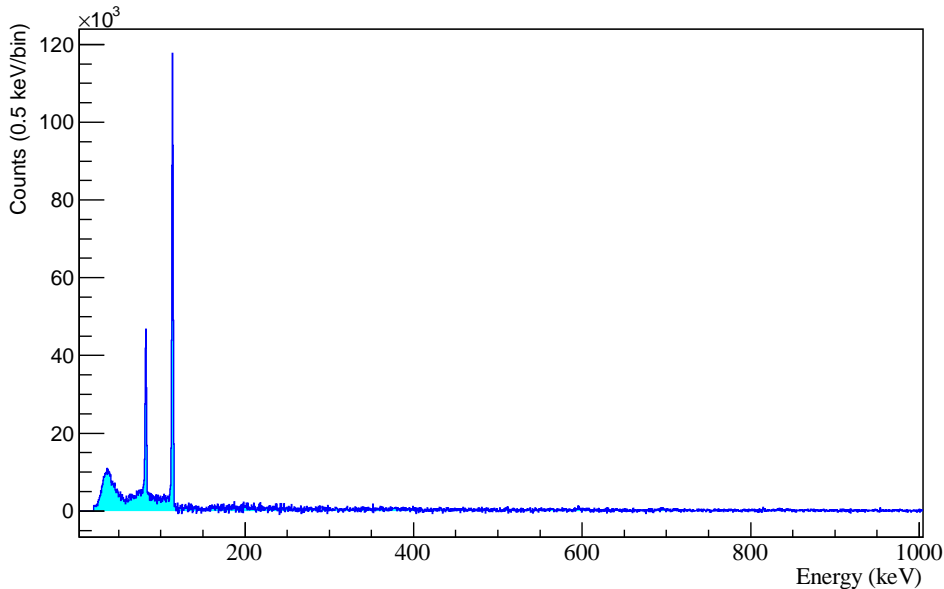
Figure 5.2: EURICA energy spectrum after background subtraction with applied time window.

5.2 Delayed-prompt analysis

To identify states on top of the isomer, e.g. in coincidence, we gate on the two isomeric transitions measured with EURICA in the merged data. For a reduced background we apply the same time window as in the previous section. The so-called isomer gate used in the following is defined by requiring a coincidence with delayed γ-rays registered in EURICA in the ranges $112.5 - 115.1$ keV or $80.4 - 83.0$ keV which represent the known 113.8 keV and 81.7 keV transitions depopulating the $(7/2)^+$ isomer in ^{95}Kr. The corresponding DALI2 energy spectrum is filled with the events matched to the

EURICA events by the merging process. The analysis is done for each reaction channel separately.

5.2.1 The $(p, 2pn)$ reaction channel

Figure 5.3: DALI2 spectrum for the (p,2pn) reaction channel in coincidence with the isomeric transitions.

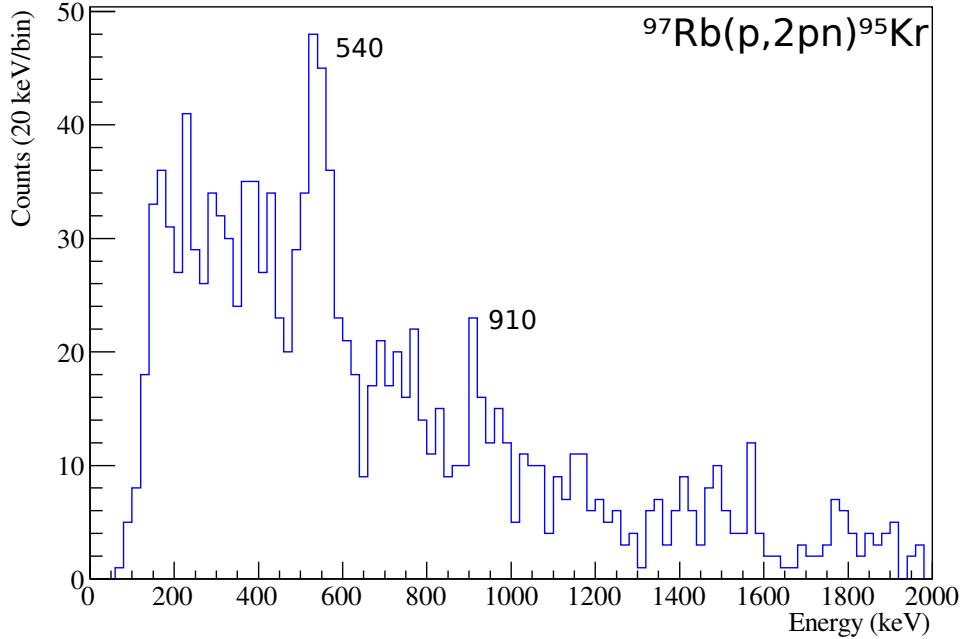The first reaction channel we look at is the $(p, 2pn)$ reaction channel. The full DALI2 spectrum coincident with the isomeric transitions in EURICA is shown in Figure 5.3. To reduce the background in the DALI2 spectra, it is possible to put a number of constraints on the data. The number of proton tracks measured with the MINOS TPC can be defined. In Figure 5.3 only events with two protons observed in the TPC are included. The multiplicity of the event, e.g. the number of detectors active in one event, can also be restricted. A multiplicity of ≤ 5 was used for all DALI2 data if not otherwise denoted. In the resulting energy spectrum, we see a very strong coincident transition at $\sim 540\,\mathrm{keV}$ and a narrow coincident transition at $\sim 910\,\mathrm{keV}$. For more information on the level structure on top of the isomer, prompt $\gamma\gamma$-matrices in coincidence with the isomeric transitions were built. Then, together with the gate in EURICA, different gates were set in the DALI2 matrix to identify γ-cascades.

In Figure 5.4, the DALI2 spectra for 30 keV gates on $540\,\mathrm{keV}$ (Fig. 5.4 a)) and on $910\,\mathrm{keV}$ (Fig. 5.4 b)) are displayed. Both show a coincident transition at $1405\,\mathrm{keV}$.
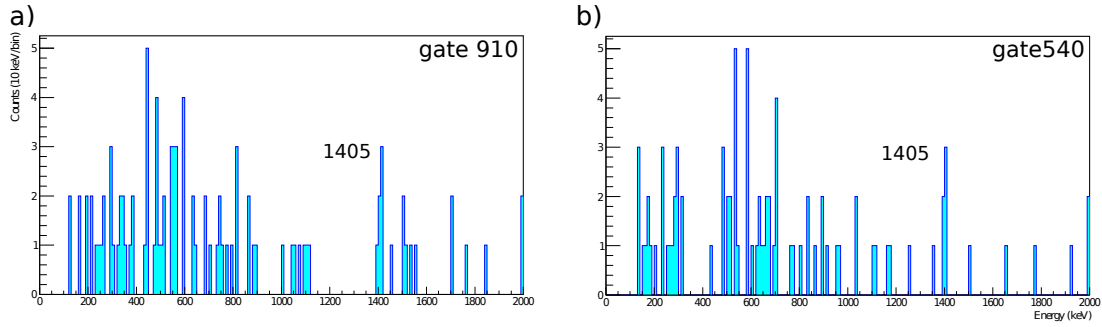
Figure 5.4: a) Spectrum with an isomer gate in EURICA and a DALI2 gate on 910 keV. b) Spectrum with an isomer gate in EURICA and a DALI2 gate on 540 keV.

To verify the coincidences, we gate in the other direction on 1405 keV. The resulting DALI2 spectrum is shown in Figure 5.5.
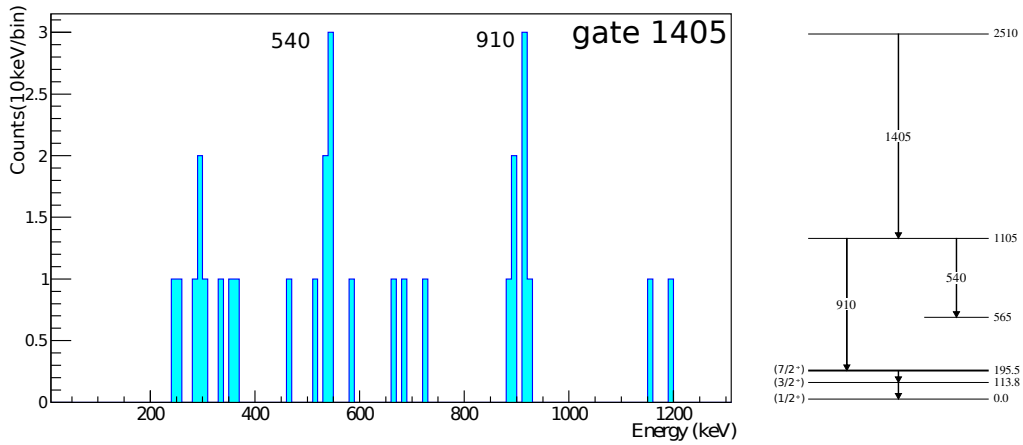

Figure 5.5: DALI2 spectrum with an isomer gate in EURICA and a DALI2 gate on 1405 keV. A tentative partial level scheme is shown on the right.

Weak coincident structures are present at the corresponding energies of 540 keV and 910 keV.

On the right side, a tentative partial level scheme is displayed with three new transition energies at 540(15) keV, 910(15) keV and 1405(15) keV. The ordering of the transitions results from their intensities in the full DALI2 spectrum in coincidence with the isomeric transitions as shown in Figure 5.3. The gate on 1405(15) keV gives the coincident transitions 540 keV and 910 keV with roughly the same intensity (see Fig. 5.5). In the full spectrum, however, we can see the 540 keV transition with a much higher intensity compared with the 910 keV transition. Therefore, we propose the presence of a second transition of approximately 540 keV in coincidence with the isomeric transitions. This transition directly decays to the isomeric state at 195.5 keV and is not coincident with the 1405(15) keV transition. In the partial level scheme in Figure 5.5, there is one unobserved transition of approximately 370 keV between the 540(15) keV transition and

the isomeric state at 195.5 keV. One would expect to observe this missing transition in the spectrum gated on 540(15) keV, shown in Figure 5.4 b). Since this is not the case, the unobserved transition could be attributed to the tentative 565 keV level being a second isomer if one assumes a half life of $1\,\text{ns} \lesssim \text{T}_{1/2} \lesssim 100\,\text{ns}$.

For the energy transitions obtained by the coincidence analysis of the merged data in this and the following section and of the DALI2 data in Section 5.3.2, there is no obvious way to determine the uncertainties of the transition energies. For a rough estimation, we used the centroids of the transition energies in the coincidence spectra with an error of one and a half of the binning, respectively. Even though this may lead to an overestimation of the uncertainties, there is no possibility to securely reduce the errors in a cohesive manner.

5.2.2 The (p, p') reaction channel

In the next step, we look at is the (p, p') inelastic scattering channel. This channel has higher statistics than the (p,2pn) and (p,pn) channels but includes a very high atomic background at low γ-ray energies. For in-beam γ-spectroscopy at high beam energies, atomic processes are the main source of background. These processes include primary bremsstrahlung, which denotes the capture of a target electron into continuum states of the beam nuclei, secondary bremsstrahlung, which corresponds to the stopping of high energy electrons in the target, and the radiative capture of electrons into bound states of the beam particles.

Generally, in the case of (p,p') inelastic scattering, the proton involved in the reaction is not observed in the TPC because the momentum transfer is too small. Therefore, the DALI2 spectrum coincident with the isomeric transitions shown in Figure 5.6 only includes events where zero protons were observed. Additionally, it is possible to improve the spectra by removing certain detector layers containing a high background. In Figure 5.6 only data from 92 NaI detectors is shown, excluding detector layers covering large backward angles.

The DALI2 spectrum in Figure 5.6 is dominated by atomic background but, nevertheless, we can identify structures related to coincident transitions. Like in the previous section, we built $\gamma\gamma$-matrices for further information.

Figure 5.7 a) is obtained with a 30 keV DALI2 gate on 960 keV while the spectrum in Figure 5.7 b) is gated on 565 keV. With the additional EURICA gate on the two isomeric transitions, we can deduce a tentative level scheme shown on the right side with two coincident transitions at 565(15) keV and 960(30) keV. Like in the previous
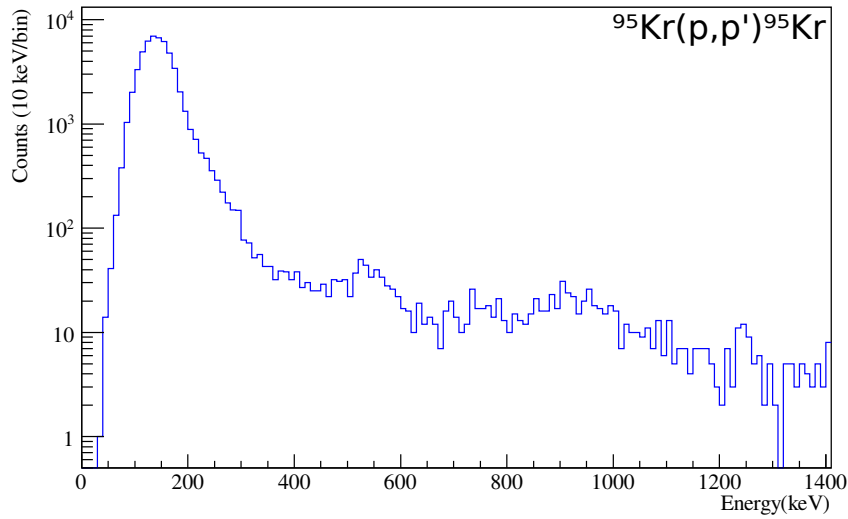
Figure 5.6: DALI2 spectrum for the (p,p') reaction channel in coincidence with the isomeric transitions.
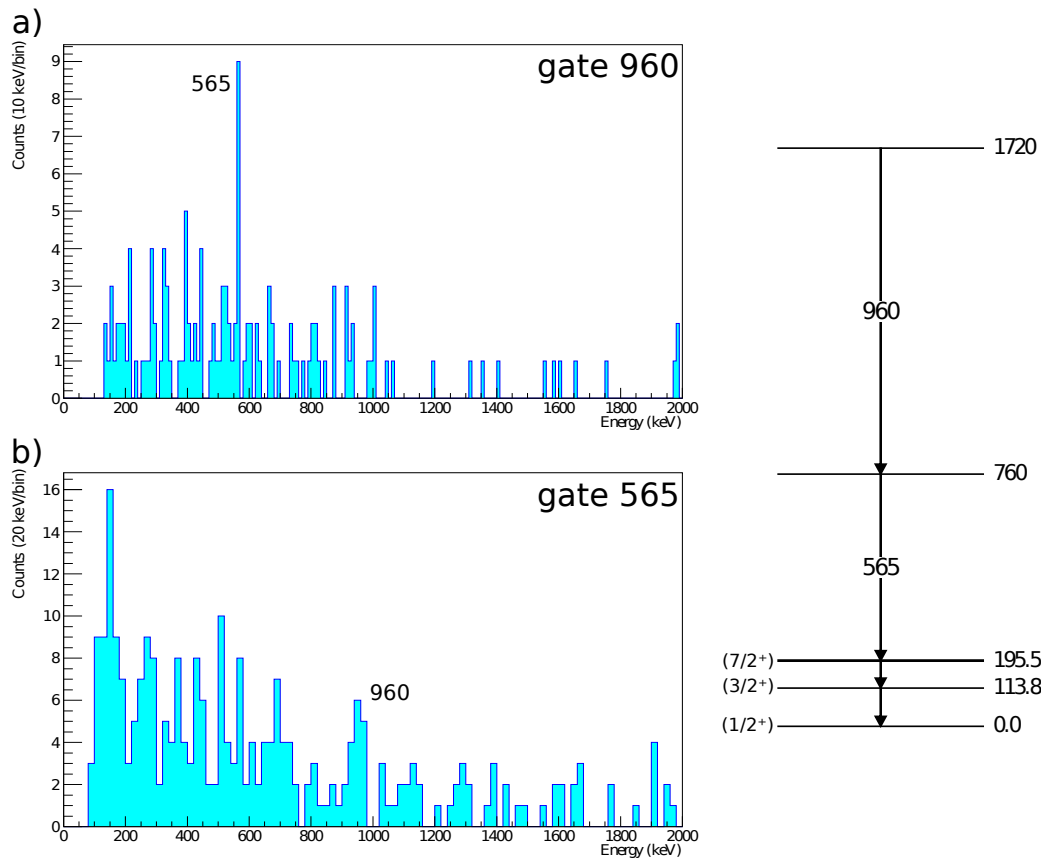
Figure 5.7: a): Spectrum with an isomer gate in EURICA and a DALI2 gate on 960 keV. b) Spectrum with an isomer gate in EURICA and a DALI2 gate on 565 keV. A tentative level scheme is shown on the right.

section, the ordering of the transitions is chosen with respect to their intensities in the full DALI2 spectrum in coincidence to the isomeric transitions (Fig. 5.6).

The DALI2 energy spectrum for a 20 keV gate on 930 keV is displayed in Figure 5.8 a). Below, in Figure 5.8 b), we see the spectrum for a 20 keV gate on 540 keV.
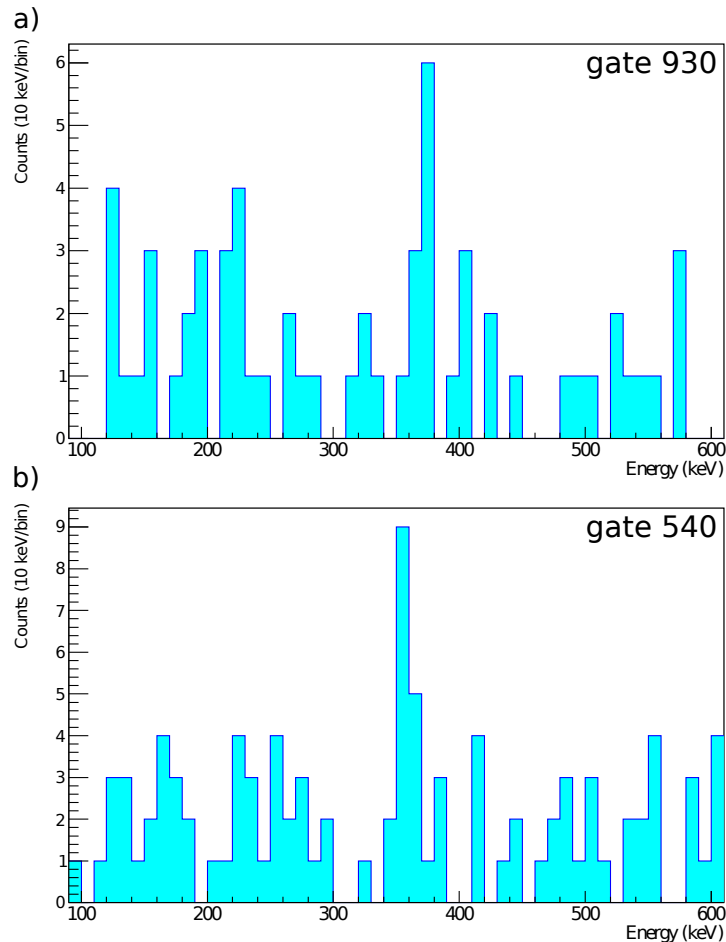
Figure 5.8: a) Spectrum with an isomer gate in EURICA and a DALI2 gate on 930 keV. b) Spectrum with an isomer gate in EURICA and a DALI2 gate on 540 keV.

The resulting coincident transitions for the two gates are very close to each other. To prove that these are indeed two different energy transitions, we set two different 10 keV gates, one on 355 keV and one on 375 keV. The resulting energy spectra are shown in Figure 5.9. The two gates clearly show different results in agreement with Figure 5.8. A corresponding tentative level scheme is shown on the right side of Figure 5.9 with four new transition energies at 355(15) keV, 375(15) keV, 540(15) keV and 930(15) keV. As before, the ordering of the transitions is chosen due to their intensities. In the full DALI2 energy spectrum shown in Figure 5.6, we don't observe the 355 keV and 375 keV transitions while we can clearly make out the 540(15) keV and 930(15) keV transitions. The arrangement of the transitions also supports the observations in the (p,2pn) reaction channel where we proposed a 540 keV transition directly on top of the isomeric state.
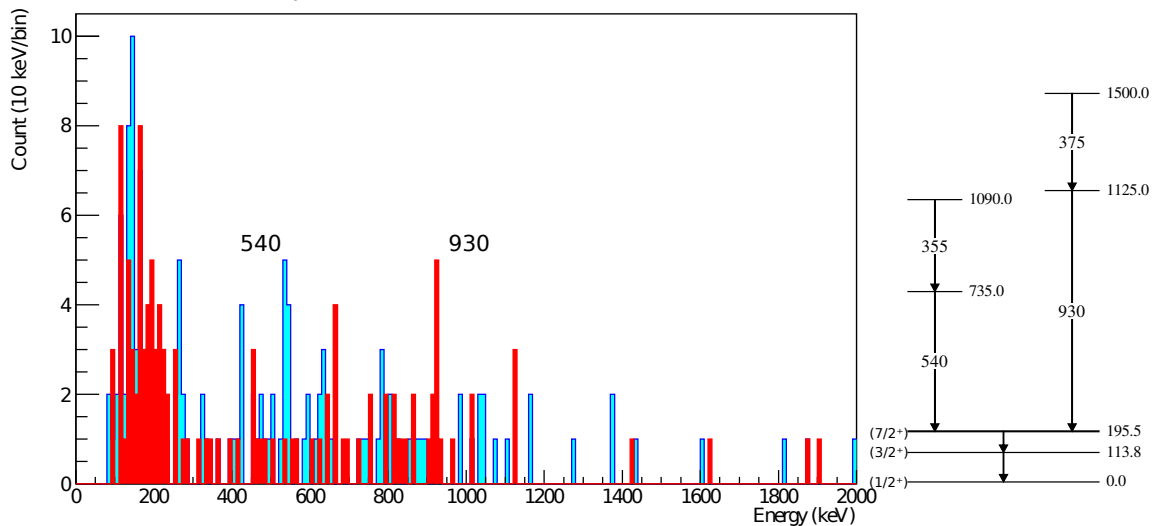
Figure 5.9: Spectrum with an isomer gate in EURICA and two different DALI2 gates: 355 keV (blue) and 375 keV (red). A tentative level scheme is shown on the right.

5.2.3 The (p, pn) reaction channel
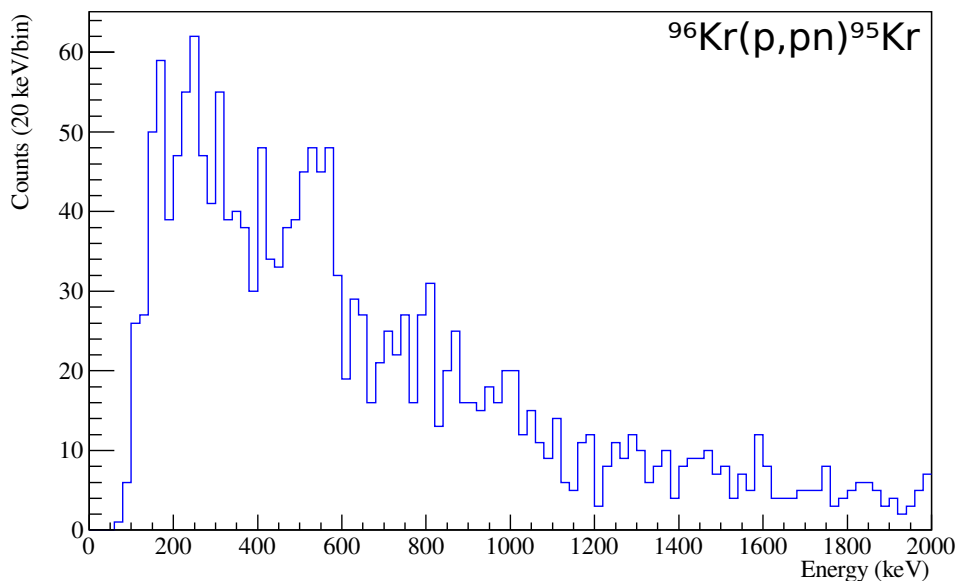
**Figure 5.10:** DALI2 spectrum for the (p,pn) reaction channel in coincidence with the isomeric transitions.

The DALI2 energy spectrum in coincidence with the isomeric transitions in EURICA for the (p,pn) reaction channel is shown in Figure 5.10. Like for the (p,2pn) reaction, one observes a peak around 540 keV which, for this reaction, is less pronounced. Though the reaction has slightly higher statistics, the $\gamma\gamma$-matrix does not yield any conclusive results on the level structure coincident with the isomer.

5.2.4 Discussion
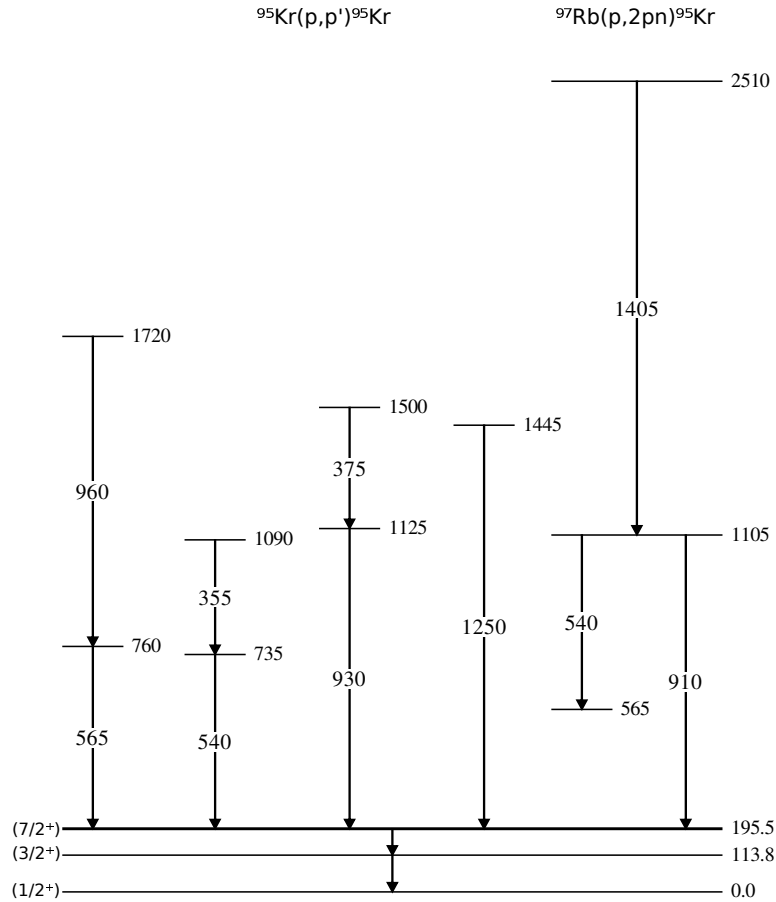
Figure 5.11: Tentative level scheme of ^{95}Kr considering all transition energies observed with DALI2 in coincidence with the isomeric transitions measured with EURICA.

All transition energies, that were observed in coincidence with the isomeric transitions in the (p,p') and (p,2pn) reaction channels, are shown in a combined tentative level scheme in Figure 5.11. In Section 5.2.1, we proposed the presence of two transitions of approximately 540 keV in coincidence with the isomeric transitions due to the high intensity of the corresponding peak in the full coincident energy spectrum. This is corroborated by the observation of a 540(15) keV transition in the (p,p') reaction channel. Both 540 keV transitions are shown in Figure 5.11 with their respective coincident transitions. The 355 keV transition is only observed coincident with the 540(15) keV transition in the (p,p') reaction. Therefore, we can assume that the tentative 1090 keV level is not populated in the (p,2pn) reaction. The unobserved transition between the tentative 565 keV level and the isomeric 7/2$^+$ state would be around 370 keV. This energy lies within the uncertainties of two transitions observed in the (p,p') channel, 355(15) keV and 375(15) keV, which are not found in the (p,2pn) channel. Due to their respective intensities, in Section 5.2.2, we proposed that these two transitions do not directly decay to the isomeric state but are arranged as shown in Figure 5.11. There-

47

fore. we assume that neither of these transitions corresponds to the unobserved one. As we have discussed previously, a second isomer is expected on top of the $(7/2^+)$ isomer at 195.5 keV. The missing transition, therefore, could be attributed to the decay from this second isomer. For this isomer at approximately 565 keV a half life of $1\,\mathrm{ns} \lesssim T_{1/2} \lesssim 100\,\mathrm{ns}$ would have to be assumed. With the available data, no assumptions can be made with certainty. More precise measurements are needed for a certain attribution and arrangement of the observed transitions.

5.3 DALI2 analysis

After the analysis of the merged data, we take a look at the DALI2 data separately. In Figure 5.12, the DALI2 energy spectra for the (p,2pn) (top) and the (p,pn) (bottom) reaction channels are shown. The (p,p') inelastic reaction channel contains a very high background and the analysis of the unmerged prompt data in this channel has not yielded any conclusive results.

From the differences of the spectra of the two reaction channels one can try to draw conclusions about the nature of the measured transition energies. For the (p,pn) reaction channel, we dominantly assume neutron excitations while for the (p,2pn) reaction, neutron and proton excitations are expected equally. In a rather simplified view, we can therefore deduce that the strong transition at 250 keV, which is present in both spectra but has a higher relative intensity for the (p,pn) reaction, is related to excited neutron states. On the other hand, we can deduce that transition energies, which are dominantly observed in the (p,2pn) reaction channel, are caused by proton excitation. Another difference to consider is the nuclear structure of the initial secondary nuclei before the knockout reactions, i.e. ^{96}Kr in its ground state can be considered as slightly deformed [2] while ^{97}Rb already has a stronger deformation as shown by mass measurements, Coulomb excitation and nuclear structure models accounting for the known level energies and transition strengths [38].

The energy spectra shown in Figure 5.12 indicate more and differing transition energies than observed in coincidence with the isomeric transitions. To prove that these transitions do not decay to the isomeric state, we go back to the combined data from EURICA and DALI2. Instead of gating on the isomeric transitions in the EURICA data, we now set gates on different energy regions in the DALI2 data. Two examples of the resulting energy spectra for the (p,2pn) reaction channel are shown in Figure 5.13.

In Figure 5.13 a), we see the EURICA energy spectrum for a wide DALI2 gate on the structure around 250 keV and in Figure 5.13 b) for a wide gate on the structure around
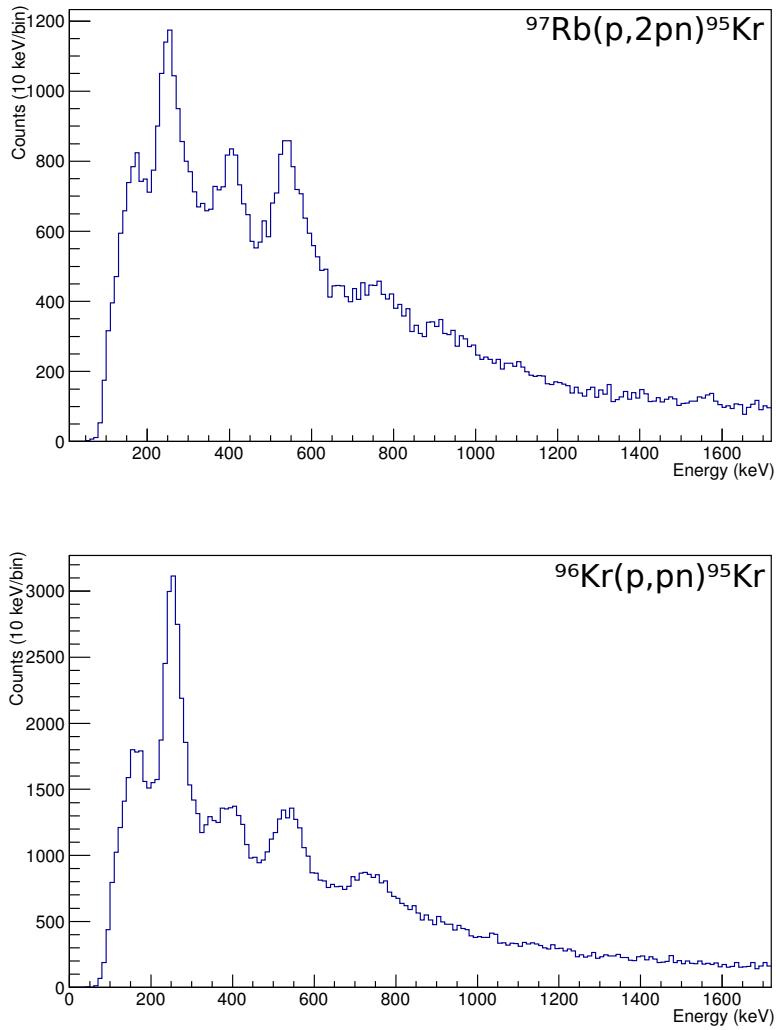
Figure 5.12: DALI2 energy spectra for γ-multiplicities ≤ 5. Top: The (p,2pn) reaction channel. Bottom: The (p,pn) reaction channel.
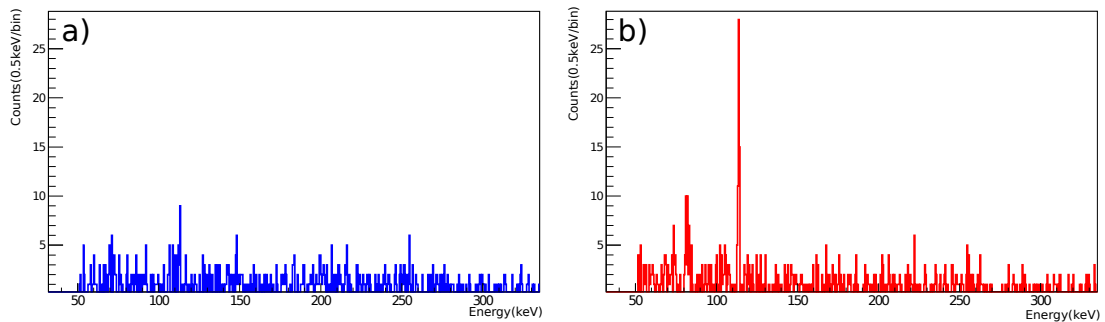
Figure 5.13: EURICA energy spectrum with the DALI2 gates a) $220 - 280\,\mathrm{keV}$ and b) $520 - 580\,\mathrm{keV}$ for the (p,2pn) reaction channel.

$540\,\mathrm{keV}$ including the $540(15)\,\mathrm{keV}$ and $565(15)\,\mathrm{keV}$ transition energies previously shown to be coincident with the isomer. Accordingly, we can clearly see the coincident isomeric transitions in Figure 5.13 b) while Figure 5.13 a) shows no coincident transitions to

the 250 keV gate set in DALI2. We can therefore assume that the prominent peak in the 250 keV energy region predominantly includes transitions that do not decay to the isomeric state at 195.5 keV.

5.3.1 Geant4 simulations

To determine the individual transition energies which generate the energy spectra of Figure 5.12, we perform Geant4 simulations [31] for both reaction channels.

Figure 5.14: Geant4 response function for a transition energy of 540 keV.

With the Geant4 code, it is possible to obtain reliable values of energy resolutions and detection efficiencies and simulate realistic γ-ray line shapes taking into account the target thickness and possible life 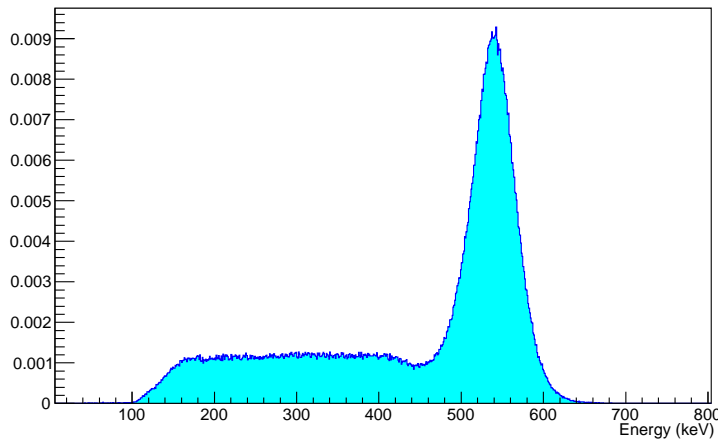times of excited states. The simulation process is separated in three distinct steps. For each transition energy included, the Geant4 Event Generator first simulates the reaction of the ion beam in the 100 mm LH$_2$ target and the emission of the γ-ray. Afterwards, the Event Builder simulates the detection response of the DALI2 detectors and the Reconstructor performs the Doppler correction and add-back procedure. Thereby, we obtain response functions for each transition energy entered. The simulated response function for a prompt 540 keV transition is shown in Figure 5.14. In the next step, these response functions are used to reproduce the whole DALI2 energy spectrum.

5.3.1.1 The $(\mathrm{p}, 2\mathrm{pn})$ reaction channel

In Figure 5.15, the full simulation of the DALI2 energy spectrum for the (p,2pn) reaction channel is shown.

50
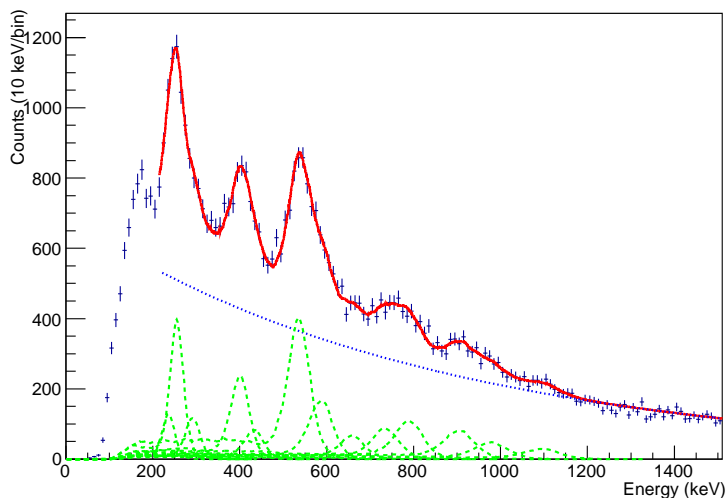
E (keV)	I_rel
235(10)	13(3)
254(4)	44(4)
291(12)	15(2)
400(6)	43(4)
432(20)	16(3)
536(3)	100(5)
586(7)	47(4)
657(16)	21(3)
734(16)	31(3)
788(9)	43(4)
903(11)	37(4)
978(21)	24(4)
1093(21)	17(3)

Figure 5.15: DALI2 spectrum for the ^{97}Rb(p, 2pn)^{95}Kr reaction channel: Experimental data points, the simulated response for each transition (green), the two-exponential background (blue), and the sum of these simulated peaks with this background (red). Multiplicities ≤ 5 are shown. The transition energies and relative intensities of the simulated peaks are displayed in the table.

This result is obtained in several steps. First, one has to choose suitable transition energies for the reproduction of the spectrum. The response functions of these energies, together with a two-exponential background for high and for low energies, is used for the simulation. The code can modify the included transition energies by shifting their energy and adjusting their gain. Starting at high energies, the included transition energies are optimised step by step until no input energy is shifted by the simulation. We don't use the whole energy range for the simulation. The combined effect of the atomic background and the detection threshold distorts the spectrum at very low energies. Therefore, we only include data with energies $\gtrsim 200\,$keV in the simulation, as can be seen in Figure 5.15.

For further optimisation, we then generate χ^2 distributions of the simulation for each energy. With all other parameters fixed, we vary one input energy of the simulation in $1\,$keV steps. For each energy, a new response function has to be simulated as described in the previous section. The thereby obtained χ^2 distributions are then fitted to find the energy corresponding to a minimal χ^2. One example is shown in Figure 5.16. With a starting value of $780\,$keV, an optimised value of $788\,$keV was obtained as the minimum of the χ^2 distribution. This minimisation process is performed for each input transition energy separately. The optimised energies are then used for the simulation of the whole spectrum. The final result for the (p,2pn) reaction is shown in Figure 5.15 with all included transition energies shown together with their relative intensities in the table
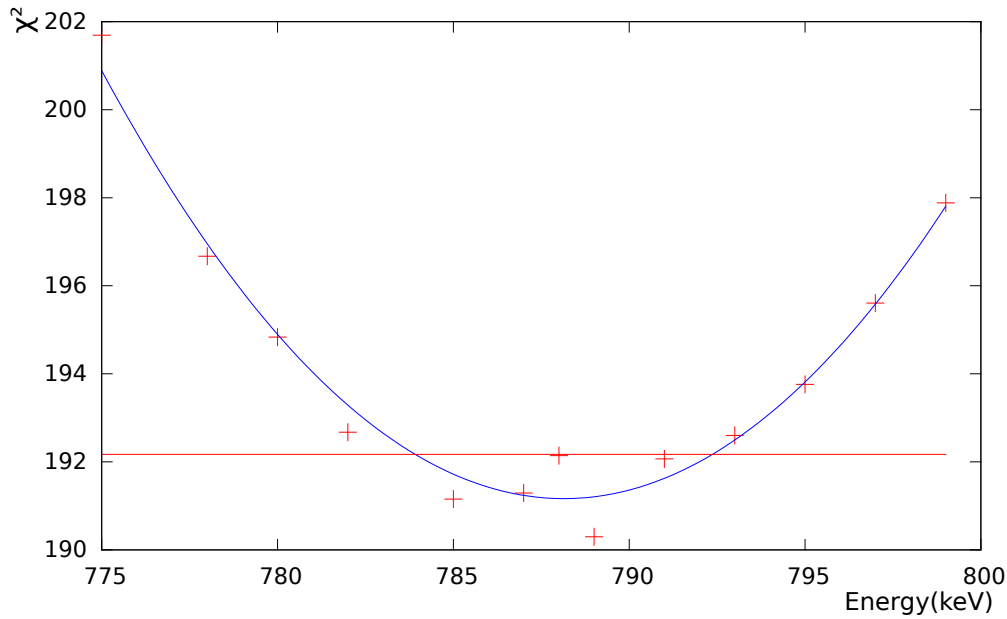
on the right side.

Figure 5.16: χ^2 distribution for the 788 keV transition energy with the 1σ level marked by the red line.

The errors of the final transition energies of the simulation are obtained from the 1σ level of the χ^2 distributions, as marked in Figure 5.16 by the red line, and the calibration error of 1 keV. Possible life times of the excited states can also have a large influence on the simulations since the emission points of the γ-rays are shifted compared to the reaction vertex position. On account of this, the peak positions are shifted towards lower energies and reconstructed with an asymmetric form. The inclusion of a life time of 50 ps in the simulation of the response function causes a shift in energy of 6 keV for 254 keV, 12 keV for 536 keV and 20 keV for 903 keV. The χ^2 minimisation, which was done with respect to the transition energy, also has to be performed for the lifetime of the decaying energy level. Generally, the energy uncertainties are dominated by these life time effects. This last step has not yet been finalised for the simulations in this analysis.

5.3.1.2 The (p, pn) reaction channel

The DALI2 energy spectrum for the (p,pn) reaction channel was simulated as described in the previous section. Instead of choosing seemingly suitable transition energies, we preferably used the optimised energies of the simulation for the (p,2pn) reaction channel. The resulting simulation is shown in Figure 5.17 together with the experimental data. The transition energies and their relative intensities are displayed on the right side. For the reproduction of this spectrum, the response functions for 1093 keV,
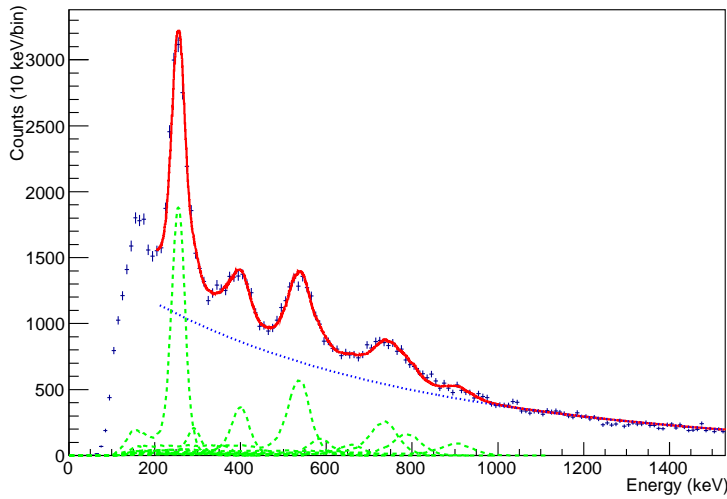
E (keV)	I_{rel}
254(4)	100(2)
291(12)	12(2)
360(10)	6(2)
400(6)	31(2)
536(3)	69(2)
586(7)	17(1)
657(16)	12(1)
734(16)	44(2)
788(9)	30(2)
903(11)	20(2)

Figure 5.17: DALI2 spectrum for the ^{96}Kr(p, pn)^{95}Kr reaction channel: Experimental data points, the simulated response for each transition (green), the two-exponential background (blue), and the sum of these simulated peaks with this background (red). Multiplicities ≤ 5 are shown. The transition energies and relative intensities of the simulated peaks are displayed in the table.

978 keV, 432 keV and 235 keV, which were necessary for the (p,2pn) channel, were not used and one additional transition energy of 360 keV was included. One can therefore assume that the former transitions are related to excited proton states while the latter corresponds to neutron excitation.

5.3.2 $\gamma\gamma$-coincidence analysis

In the final part of the DALI2 analysis, a coincidence analysis was performed for the (p,2pn) and the (p,pn) reaction channels. $\gamma\gamma$-matrices for the respective reaction channels were built and γ-gates of varying width were set covering the whole measured energy range to determine conclusive coincidences. While the level scheme of ^{95}Kr appears to be very complex, only the most distinct transitions with clear coincidences in both directions are presented.

In Figures 5.18 and 5.19, a group of coincident transition energies is displayed which can be observed in the (p,2pn) and the (p,pn) reaction channel. The gated spectra for the (p,2pn) channel are shown in Figure 5.18. The observed transition energies are 255(15) keV, 290(30) keV, 780(30) keV and 970(15) keV.

The gated spectra for the (p,pn) reaction channel are shown in Figure 5.19. For this channel, we obtain the transition energies 255(15) keV, 290(30) keV, 780(30) keV and 1995(30) keV. The former three energies are observed in both reaction channels with
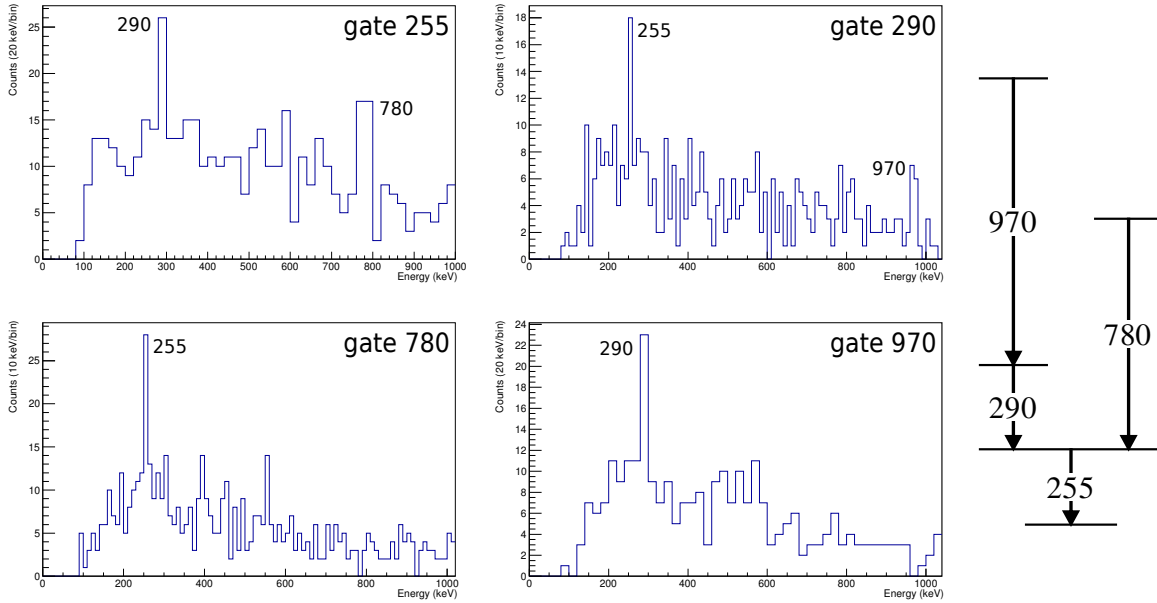
Figure 5.18: DALI2 energy spectra for different gates in the (p,2pn) channel. Coincidences are shown for the transition energies 255(15) keV, 290(30) keV, 780(30) keV and 970(15) keV with the corresponding partial tentative level scheme on the right.

Figure 5.19: DALI2 energy spectra for different gates in the (p,pn) channel. Coincidences are shown for the transition energies 255(15) keV, 290(30) keV, 780(30) keV and 1995(30) keV with the corresponding partial tentative level scheme on the right.

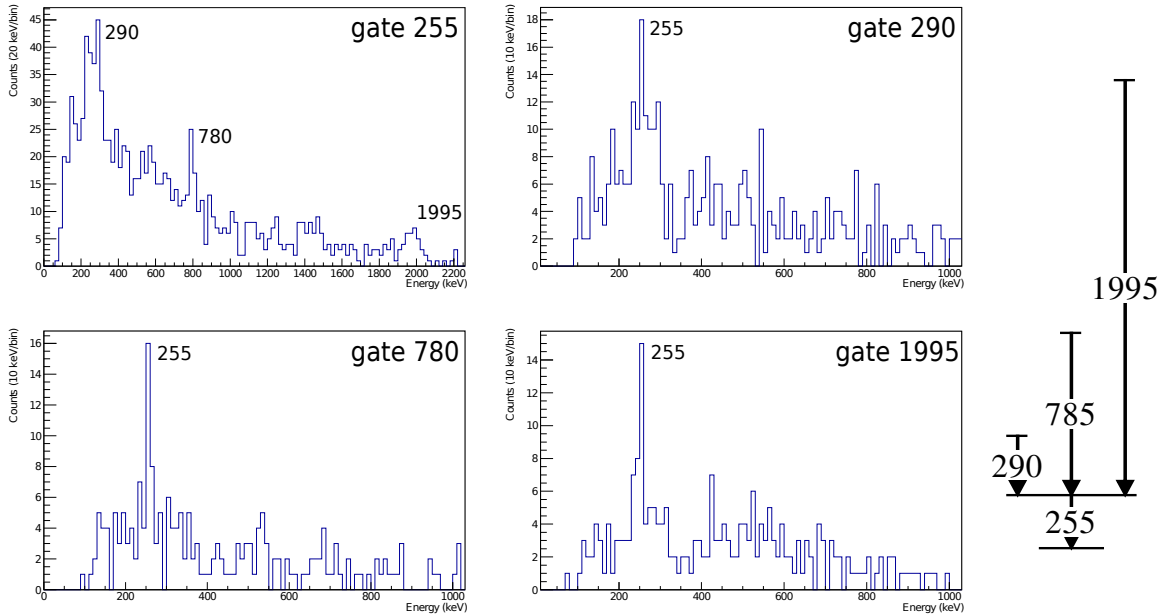the same coincidence results. There is one additional transition at 1995(30) keV for the (p,pn) reaction and one at 970(15) keV for the (p,2pn) reaction. The decay schemes in Figures 5.18 and 5.19 are arranged with respect to the observed coincident transitions

and their intensities in the Geant4 simulations of the full energy spectra shown in Figures 5.15 and 5.17.

All other conclusive coincidences, which will be discussed subsequently, were only observed in one of the reaction channels. Figure 5.20 displays two coincident transitions with the energies 405(15) keV and 670(15) keV. Even though these transition energies are both part of the Geant4 simulations for the (p,pn) and (p,2pn) reaction channels, the coincidence between them is only observed in the (p,pn) channel. The ordering of the two transitions, as displayed in the tentative decay scheme in Figure 5.20, is due to their relative intensities in the Geant4 simulation shown in Figure 5.17.
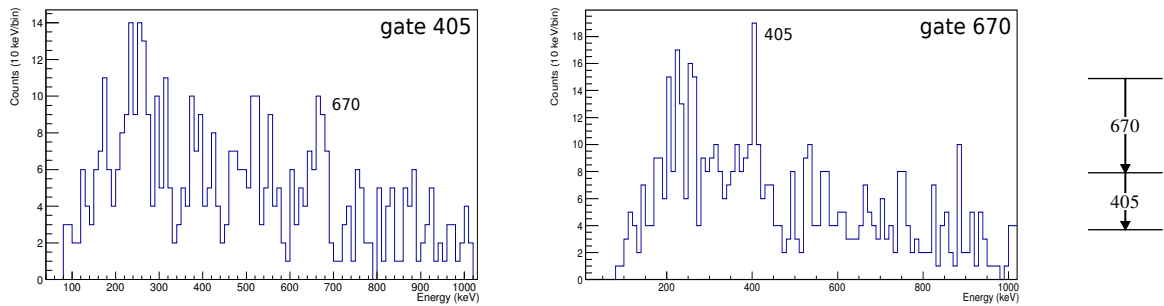

Figure 5.20: DALI2 energy spectra for different gates in the (p,pn) channel. Coincidence spectra for the transition energies 405(15) keV and 670(15) keV with the corresponding decay scheme on the right.

The coincidences observed in the (p,2pn) reaction channel are shown in Figure 5.21. From these, we obtain the transition energies: 235(15) keV, 560(15) keV, 875(15) keV (Fig. 5.21 a)), 740(15) keV, 1540(30) keV (Fig. 5.21 b)), 390(15) keV, 800(15) keV (Fig. 5.21 c)), 310(30) keV and 530(30) keV (Fig. 5.21 d)). The corresponding decay schemes are displayed on the right side.

In principle all of the transition energies obtained from the coincidence analysis of the different reaction channels should correspond to transition energies included in the Geant4 simulations for the full energy spectra described in Section 5.3.1. The transition energies 255(15) keV, 290(30) keV, 405(15) keV, 530(30) keV, 670(15) keV, 740(15) keV and 780(30) keV, for example, all lie within the uncertainty of the fitted energies 254(4) keV, 291(12) keV, 400(6) keV, 536(3) keV, 657(16) keV, 734(16) keV and 788(9) keV of the Geant4 simulations for both reaction channels. However, while these transitions were included in the simulations for both reactions, in the coincidence analysis, some were only observed in one of the reactions. The transitions 235(15) keV and 970(15) keV, which were only observed in the (p,2pn) reaction channel, can be assumed to correspond to the Geant4 energies 235(15) keV and 987(21) keV, which were only used for the simulation of the (p,2pn) energy spectrum.
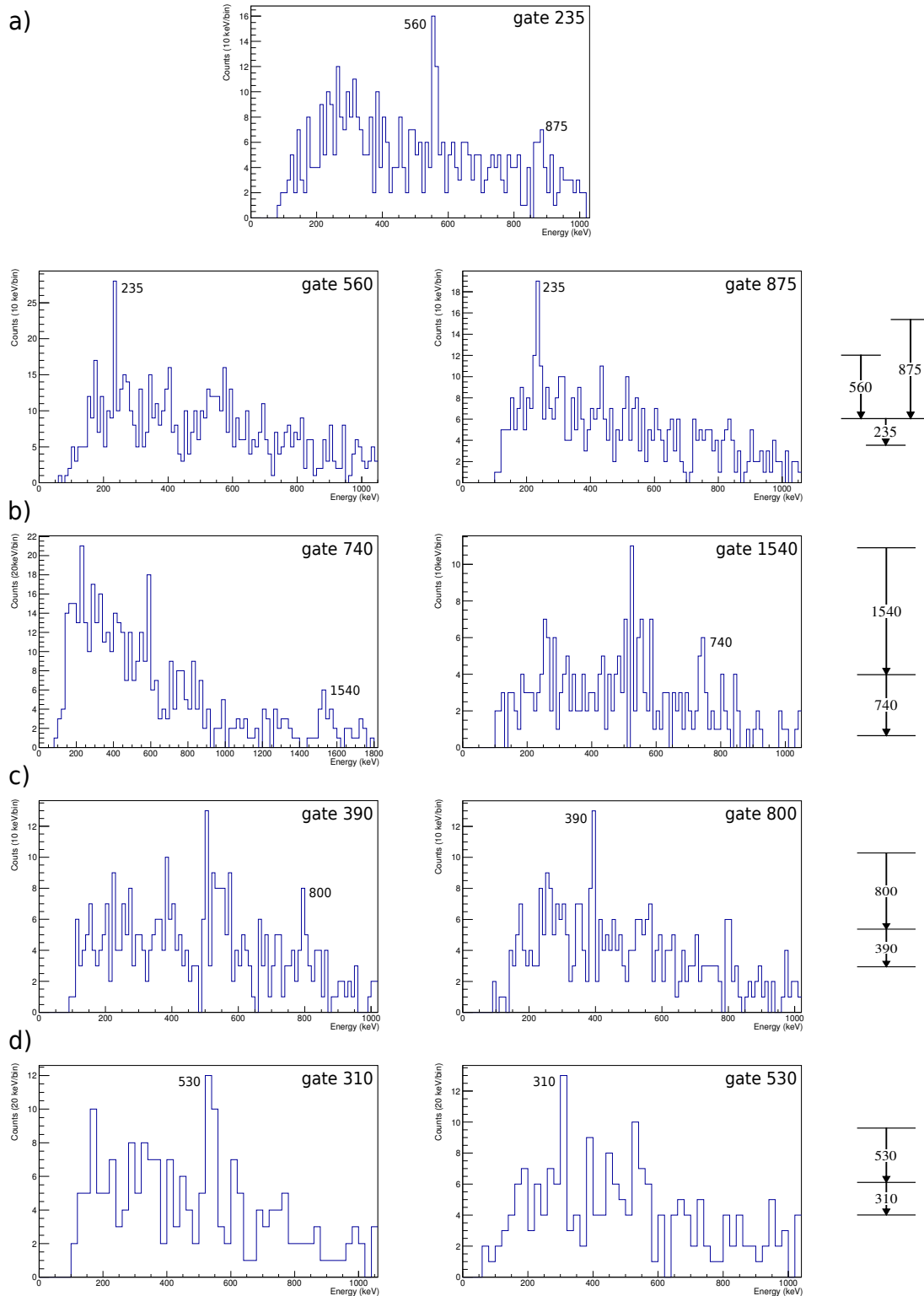
Figure 5.21: DALI2 energy spectra for different gates in the (p,2pn) channel: a) Coincidence spectra for the transition energies 235(15) keV, 560(15) keV and 875(15) keV. b) Coincidence spectra for the transition energies 740(15) keV and 1540(30) keV. c) Coincidence spectra for the transition energies 390(15) keV and 800(15) keV. d) Coincidence spectra for the transition energies 310(30) keV and 530(30) keV. The corresponding tentative decay schemes are shown on right.

In Figure 5.21, there are however also coincident transitions that are not included in the Geant4 simulations of the full spectra. One can assume that, while these transitions are present in the DALI2 energy spectra, they have lower intensities than the ones included in the simulations for the reproduction of the experimental data. The transitions $560(15)\,\mathrm{keV}$ and $390(15)\,\mathrm{keV}$ lie within the errors of transitions that were shown to be in coincidence with the isomeric transitions in Section 5.2. The energies coincident with these two transitions, shown in Figure 5.21 a) and c), on the other hand were not observed during the prompt-delayed analysis. Further analysis will be done for a better cohesive understanding of these results.

6 Summary

In-beam and decay spectroscopy of ^{95}Kr was conducted using data taken during the second SEASTAR campaign at the Radioactive Ion Beam Factory at the RIKEN Nishina Center. The isotope was populated by the ^{95}Kr(p, p$'$), ^{96}Kr(p, pn) and ^{97}Rb(p, 2pn) reactions. To investigate the level structure on top of the known $(7/2^+)$ isomer, a prompt-delayed coincidence analysis was performed by combining the SEASTAR experimental setup, including BigRIPS and the ZeroDegree spectrometer, DALI2 and MINOS, with the EURICA array as ancillary detector. The merging of these two data sets was successfully implemented for the first time. γ-spectroscopy of transitions on top of the only previously known excited states and of prompt transitions was successfully performed for the first time in ^{95}Kr.

Ten γ-transitions, measured with the DALI2 array, could be tentatively identified in the merged data in coincidence with the two known isomeric transitions. For the new transitions, a preliminary level scheme is presented in Figure 5.11 where the unobserved transition from the tentative 565 keV level might indicate the existence of a second isomer which is expected to exist in ^{95}Kr. A detailed stand alone analysis of the EURICA data will be conducted to further investigate this possibility.

Geant4 simulations were performed for the analysis of the prompt DALI2 data. The full energy γ-spectra of the (p,2pn) and the (p,pn) reaction channels were reproduced by simulations using a two-exponential background combined with the response functions of 13 and 10 γ-transitions, respectively. Conducting a $\gamma\gamma$-coincidence analysis of the prompt data showed coincidence relations between some of these tentative γ-transitions and revealed some additional ones. Due to some ambiguities, additional analysis of the available data is still needed. Nevertheless, it is clear that the low resolution of the prompt γ-spectra poses a limit on the information which can be extracted.

Therefore, further experimental studies will be necessary for a more precise determination of the nuclear structure in ^{95}Kr. Preferably, theoretical predictions are used to support and expand experimental results. Due to the large phase space of the even-odd ^{95}Kr isotope, theoretical calculations shape up to be very complex and have not been performed yet. K. Nomura (University of Zagreb), who works on a microscopical based Interacting Boson Model applicable for neutron rich Krypton isotopes, has very recently developed methods to apply this approach to odd nuclei [39] and will

conduct calculations for ^{95}Kr. Additionally, Monte Carlo shell model calculations were recently implemented in this mass region for the first time [40] and in principle could be extended to ^{95}Kr.

Further investigation of the isotope will be proposed by us soon, like for example using the high resolution HPGe spectrometer MINIBALL and HIE-ISOLDE to provide the radioactive ^{95}Kr beam.

Bibliography

[1] K. H. Heyde and J. L. Wood, Rev. Mod. Phys. **83**, 1467 (2011).

[2] M. Albers *et al.*, Phys. Rev. Lett. **108**, 062701 (2012).

[3] J. A. Pinston *et al.*, Phys. Rev. C **71**, 064327 (2005).

[4] J. K. Hwang *et al.*, Phys. Rev. C **67**, 054304 (2003).

[5] A. Złomaniec *et al.*, Phys. Rev. C **72**, 067302 (2005).

[6] S. Brant, G. Lhersonneau, and K. Sistemich, Phys. Rev. C **69**, 034327 (2004).

[7] W. Urban *et al.*, Eur. Phys. J. A **16**, 11 (2003).

[8] J. Genevey *et al.*, Phys. Rev. C **73**, 037308 (2006).

[9] W. Urban *et al.*, Eur. Phys. J. A **22**, 241 (2004).

[10] T. Kubo *et al.*, Prog. Theor. Exp. Phys., 03C003 (2012).

[11] A. Obertelli *et al.*, Eur. Phys. J. A **50**, 8 (2014).

[12] S. Takeuchi *et al.*, Nucl. Instr. Meth. A **763**, 596 (2014).

[13] P.-A. Söderström *et al.*, Nucl. Instr. Meth. B **317**, 649 (2013).

[14] M. G. Mayer, Phys. Rev. **74**, 235 (1948).

[15] O. Haxel, J. H. D. Jensen, and H. E. Suess, Phys. Rev. **75**, 1766 (1949).

[16] K. S. Krane, *Introductory Nuclear Physics* (John Wiley & Sons Inc., 1988).

[17] A. Bohr and B. R. Mottelson, *Nuclear Structure Vol. I and II*, (Advanced Book Program, 1969-1975).

[18] S. G. Nilsson, Mat. Fys. Medd. Dan. Vid. Selsk. **29** (1955).

[19] R. B. Firestone, *Table of Isotopes 8th Edition* (1999).

[20] National Nuclear Data Center: www.nndc.bnl.gov/ensdf.

[21] E. Clément *et al.*, Phys. Rev. Lett. **116**, 022701 (2016).

[22] N. Marginean *et al.*, Phys. Rev. C **80**, 021301(R) (2009).

[23] F. Flavigny *et al.*, in preparation for publication, Phys. Rev. Lett. (2017).

[24] Y. Higurashi *et al.*, Rev. Sci. Instrum. **83**, 02A333 (2012).

[25] RIBF: Introduction to RI Beam Factory and Users' Information, www.nishina.riken.jp/RIBF.

[26] Y. Yano, Nucl. Instr. Meth. B **216,** 1009 (2007).

[27] M. Bernas *et al.*, Phys. Lett. B **415**, 111 (1997).

[28] N. Fukuda *et al.*, Nucl. Instr. Meth. B **317**, 323 (2013).

[29] H. Kumagai *et al.*, Nucl. Instr. Meth. A **470**, 562 (2001).

[30] K. Kimura *et al.*, Nucl. Instr. Meth. A **538**, 608 (2005).

[31] S. Agostinelli *et al.*, Nucl. Instr. Meth. A **506,** 250 (2003).

[32] S. Chen *et al.*, submitted for publication, Phys. Rev. Lett. (2016).

[33] I. Giomataris *et al.*, Nucl. Instrum. Methods Phys. Res. A **560**, 405 (2006).

[34] H. Baba *et al.*, RIKEN Accel. Prog. Rep. **43**, 222 (2009).

[35] H. Baba *et al.*, Nucl. Instr. Meth. A **616**, 65 (2010).

[36] H. Essel *et al.*, Nuclear Science, IEEE Transactions on **43**, 132 (1996).

[37] H. Essel and N. Kurz, Nuclear Science, IEEE Transactions on **47**, 337 (2000).

[38] C. Sotty *et al.*, Phys. Rev. Lett. **115**, 172501 (2015).

[39] K. Nomura, T. Nikšić and D. Vretenar, Phys. Rev. C **93**, 054305 (2016).

[40] T. Togashi *et al.*, Phys. Rev. Lett. **117**, 172502 (2016).

Erklärung

Hiermit versichere ich, Rosa-Belle Gerst, an Eides statt, dass ich die vorliegende Arbeit selbstständig und ohne die Benutzung anderer als der angegebenen Hilfsmittel angefertigt habe. Alle Stellen, die wörtlich oder sinngemäß aus veröffentlichten und nicht veröffentlichten Schriften entnommen wurden, sind als solche kenntlich gemacht. Die Arbeit ist in gleicher oder ähnlicher Form oder auszugsweise im Rahmen einer anderen Prüfung noch nicht vorgelegt worden. Ich versichere, dass die ein- gereichte elektronische Fassung der eingereichten Druckfassung vollständig entspricht.

Rosa-Belle Gerst

23.01.2017